ELSEVIER

Contents lists available at ScienceDirect

### Remote Sensing of Environment

journal homepage: www.elsevier.com/locate/rse





## A thermal radiation directionality correction method for the surface upward longwave radiation of geostationary satellite based on a time-evolving kernel-driven model

Boxiong Qin <sup>a,b,c</sup>, Biao Cao <sup>a,c,\*</sup>, Jean-Louis Roujean <sup>d</sup>, Jean-Philippe Gastellu-Etchegorry <sup>d</sup>, Sofia L. Ermida <sup>e</sup>, Zunjian Bian <sup>a</sup>, Yongming Du <sup>a,c</sup>, Tian Hu <sup>f</sup>, Hua Li <sup>a</sup>, Qing Xiao <sup>a,c</sup>, Shuisen Chen <sup>b</sup>, Qinhuo Liu <sup>a,c</sup>

- a State Key Laboratory of Remote Sensing Science, Aerospace Information Research Institute, Chinese Academy of Sciences, Beijing 100101, China
- <sup>b</sup> Research Center of Guangdong Province for Engineering Technology Application of Remote Sensing Big Data, Guangzhou Institute of Geography, Guangdong Academy of Sciences, Guangzhou 510070, China
- <sup>c</sup> College of Resources and Environment, University of Chinese Academy of Sciences, Beijing 100049, China
- d Centre d'Etudes Spatiales de la BIOsphère (CESBIO), Toulouse III University, CNRS, CNES, IRD, INRA, 31401 Toulouse cedex 9, France
- <sup>e</sup> Inst Portugues Mar & Atmosfera IPMA, P-1749077 Lisbon, Portugal
- f Remote Sensing and Natural Resources Modeling, ERIN Department, Luxembourg Institute of Science and Technology (LIST), Belvaux, Luxembourg

### ARTICLE INFO

Edited by Jing M. Chen

Keywords:

Thermal radiation directionality correction Time-evolving Kernel Driven Model Geostationary satellite Surface upward longwave radiation ABI/GOES-16

#### ABSTRACT

Thermal radiation directionality (TRD) characterizes the anisotropic signature of most surface targets in the thermal infrared domain. It causes significant uncertainties in estimating surface upward longwave radiation (SULR) from space observations. In this regard, kernel-driven models (KDMs) are suitable to remove TRD effects from remote sensing dataset as they are computationally efficient. However, KDMs requires simultaneous multiangle observations as inputs to be well calibrated, which yields a difficulty with geostationary satellites as they can only provide a single-angle observation. To overcome this issue, we proposed a six-parameter time-evolving KDM that combines a four-parameter SULR diurnal variation model and a two-parameter TRD amplitude model to correct the TRD effect for single-angle estimated SULR dataset of geostationary satellites. The significant daytime TRD effect when solar zenith angle is within  $60^{\circ}$  can be effectively eliminated. The modeling accuracy of the time-evolving KDM is evaluated using a simulated SULR dataset generated by the 3D Discrete Anisotropic Radiative Transfer (DART) model; the TRD correction method based on the new time-evolving KDM is validated using a two-year single-angle estimated SULR dataset derived from data of the Advanced Baseline Imager (ABI) onboard Geostationary Operational Environmental Satellite-16 (GOES-16) against in situ measurements at 20 AmeriFlux sites. Results show that the proposed time-evolving KDM has a high accuracy with an  $R^2 > 0.999$  and a small RMSE  $= 1.5 \text{ W/m}^2$ ; the TRD correction method based on the time-evolving KDM can greatly reduce the GOES-16 SULR uncertainty caused by the TRD effect with an RMSE decrease of 4.5 W/m<sup>2</sup> (22.1%) and mean bias error decrease of 7.9 W/m<sup>2</sup> (62.7%). Hence, the proposed TRD correction method is practically efficient for the operational TRD correction of SULR products generated from the geostationary satellites (e.g., GOES-16, FY-4A, Himawari-8, MSG).

### 1. Introduction

Thermal radiation directionality (TRD) is an anisotropic phenomenon to be taken into account when measuring the Earth's surface simultaneously at different view angles in the thermal infrared (TIR)

spectral-domain (Monteith and Szeicz, 1962; Francois et al., 1997; Sobrino et al., 2005; Lagouarde et al., 2010; García-Santos et al., 2015; Cao et al., 2019b; Coll et al., 2019; Bian et al., 2022; Pérez-Planells et al., 2022). The TRD phenomenon was initially reported in a study about the energy balance for a range of natural surfaces (Monteith and Szeicz,

E-mail address: caobiao@aircas.ac.cn (B. Cao).

<sup>\*</sup> Corresponding author at: State Key Laboratory of Remote Sensing Science, Aerospace Information Research Institute, Chinese Academy of Sciences, Beijing 100101, China.

1962) and was subsequently investigated using in situ, aircraft, and satellite observations (Cao et al., 2019b) on a variety of land covers, including vegetation (McGuire et al., 1989; Du et al., 2007; Rasmussen et al., 2011; Bian et al., 2017; Bian et al., 2020; Liu et al., 2020a), water surfaces (Masuda et al., 1988; Sobrino and Cuenca, 1999; Cuenca and Sobrino, 2004b), bare soil (Sobrino and Cuenca, 1999; Cuenca and Sobrino, 2004a; García-Santos et al., 2012; Ermida et al., 2020) and urban areas (Lagouarde et al., 2010; Lagouarde et al., 2012; Hu et al., 2016a; Dyce and Voogt, 2018; Wang et al., 2021). Accordingly, TRD is a major and well-known factor contributing to the estimation uncertainties in the Earth's surface thermal related parameters derived from remote sensing, such as surface upward longwave radiation (SULR, defined as the sum of the surface-emitted thermal radiation and the firstorder reflected component of atmospheric downward longwave radiation in 4-100 µm) (Otterman et al., 1995; Jiao et al., 2015; Cheng and Liang, 2016; Hu et al., 2019) and the land surface temperature (LST) (Trigo et al., 2008; Vinnikov et al., 2012; Guillevic et al., 2013). However, the algorithms of existing TIR satellite products placed a disregard to the TRD effect, thereby leading to some incompatibilities between the different products.

Several studies evaluated the TRD amplitude based on different satellite products and land covers. For two geostationary satellites or one geostationary satellite and one polar-orbit satellite, Minnis and Khaiyer (2000), Trigo et al. (2008) and Guillevic et al. (2013) found that the LST differences at different viewing angles could reach 6–12 K. For one polar-orbit satellite, Hu et al. (2016a) quantified the TRD effect over cities using the Moderate Resolution Imaging Spectroradiometer (MODIS) LST product and found that the TRD amplitude can reach 9 K for the most urbanized areas. Coll et al. (2019) analyzed the TRD effect over sparsely vegetated surfaces using the double-angle Advanced Along-Track Scanning Radiometer observations and found that the surface directional brightness temperature (DBT) difference between two angles can reach 8 K during summertime. Actually, non-negligible TRD effect existed in the current satellite LST/SULR products requires special effort of modeling and correction before being used.

Physically-based radiative transfer models (Verhoef et al., 2007; Cao et al., 2018; Yang et al., 2021), geometric optical models (Pinheiro et al., 2004; Bian et al., 2022), hybrid models (Du et al., 2007; Li et al., 2022), 3D models (Gastellu-Etchegorry et al., 2015; Qi et al., 2019), semiphysical kernel-driven models (KDMs) (Vinnikov et al., 2012; Duffour et al., 2016) and empirical directional emissivity models (Garcia-Santos et al., 2014; Hu et al., 2019) have been considered to simulate and remove the TRD effect. Physically-based models (i.e., radiative transfer, geometric optical, hybrid, and 3D model) need to receive inputs about the scene structural properties (e.g., leaf area index) and the thermal status (e.g., the components of temperature), which is difficult to obtain in practice, at least at the landscape scale. At the opposite, semi-physical KDM models are directly driven by multi-angle observations, and therefore they offer the best potential to be used in satellite remote sensing applications (Cao et al., 2019b; Jiang et al., 2021). In the visible and near-infrared (VNIR) domain, the KDMs have been widely used for generating directionally adjusted reflectance/albedo product using accumulative multi-temporal observations for polar-orbiting (Schaaf et al., 2002; Roy et al., 2016) and geostationary (Geiger et al., 2008; He et al., 2019) satellites. However, the existing TIR KDMs could only be driven by the simultaneously acquired (i.e., single-temporal) multiangle observations because the LST changes with time (i.e., changing with the solar energy absorption amount). It is relatively easy to achieve a singletemporal multiangle observations from ground and airborne measurements, but more difficulty at satellite scale. The only satellite mission that provides more than one observation angle in TIR domain is the dual-angle (0° and 55°) ATSR series (including ATSR, ATSR-2, AATSR, SLSTR) (Ghent et al., 2017; Coll et al., 2019), however, the two angles are not enough to solve the existing KDMs with three or four unknow parameters.

Some TRD correction working on satellite products were reported.

They are based on existing TIR KDMs (Vinnikov et al., 2012; Ermida et al., 2017; Ermida et al., 2018) that can only be applied on multisatellite overlap areas. Until now, the TRD correction for a single satellite (either geostationary or polar-orbiting satellite) is not reported. Therefore, all widely used SULR estimation methods (e.g., the hybrid method (Wang et al., 2009) and temperature-emissivity method (Tang and Li, 2008)) could not deal with the problem of TRD effect. Although geostationary satellites can't provide instantaneously multiangle observations as required to invert existing TIR KDM, they can deliver subhourly observations under a constant viewing angle with varying solar angles. If the existing fixed-time KDM could be extended to a timeevolving KDM, the daily multi-temporal observations of a geostationary satellite could be used to achieve the TRD correction of SULR product. This is a main objective of this study to propose a six-parameter time-evolving KDM that contain a four-parameter SULR diurnal variation model (DVM) and a two-parameter diurnal dynamic TRD amplitude

The remainder of this paper is organized as follows. Section 2 presents the methodology of the time-evolving KDM and the TRD correction method. The modeling accuracy of the time-evolving KDM is validated in section 3 using simulated data; and the TRD correction method based on the time-evolving KDM is validated in section 4 using Advanced Baseline Imager (ABI) data from GOES-16 and in situ pyrgeometer measurements. Finally, the conclusions are presented in section 5.

### 2. Methodology

Theoretically, the SULR is the directional and spectral integration result of the ground leaving radiances in the upper hemisphere at a broad spectral range (usually defined in 4–100  $\mu$ m (Wang et al., 2009; Qin et al., 2020) with the unit of W/m²), which is termed as hemispherically integrated SULR (SULR<sub>hem</sub>) and can be expressed as Eq. (1):

$$SULR_{hem} = \int_{0}^{2\pi} \int_{0}^{\frac{\pi}{2}} \int_{4}^{100} I_{ground-leaving}(\lambda, \theta_{v}, \varphi_{v}) sin\theta_{v} cos\theta_{v} d\lambda d\theta_{v} d\varphi_{v} \tag{1}$$

where  $\theta_{\nu}$  and  $\varphi_{\nu}$  are the viewing zenith angle (VZA) and viewing azimuth angle (VAA),  $\lambda$  is the wavelength in the unit of  $\mu m$ , and  $I_{ground-leaving}(\lambda,\theta_{v},\varphi_{v})$  is the spectral and viewing angle-related ground-leaving radiance with the unit of W/( $\mathbf{m}^{2}\cdot\mathbf{sr}\cdot\mu\mathbf{m}$ ).

In practice, the SULR is estimated from a single-angle observation of TIR spaceborne sensor with the assumption of isothermal land surface (Tang and Li, 2008; Wang et al., 2009; Qin et al., 2020). A constant value ( $\pi$ ) is used to replace the directional integration in Eq. (1), which leads to a positive or negative bias to the  $SULR_{hem}$  value. The single-angle estimated SULR ( $SULR_{dir}$ ) can be explained as Eq. (2):

$$SULR_{dir} = \pi \int_{1}^{100} I_{ground-leaving}(\lambda) d\lambda$$
 (2)

Fig. 1 illustrates the significant difference between the SULR<sub>dir</sub> and SULR<sub>hem</sub>, showing as an angle-dependent 3D mesh surface and an angleindependent flat plane, respectively. The intersection line indicates the directions with  $SULR_{dir} = SULR_{hem}$ . The red and blue lines on the mesh surface denote the SULR<sub>dir</sub> in the solar principal plane (SPP) and cross solar principal plane (CSPP), respectively. The hot spot direction (i.e., the peak) and the nadir direction (i.e., the cross point of SPP and CSPP) can be observed in SPP. Both SPP and CSPP lines have two cross points with the intersection line. The cross point within SPP with azimuth angle equal to solar azimuth angle (SAA) + 180° is shown as a magenta triangle, whose viewing angle can be termed as  $(\theta_{\nu=\nu 1}, \phi_{\nu=\nu 1})$ . In this study, the aim of developing a novel TRD correction method is to convert the SULR<sub>dir</sub> to SULR<sub>hem</sub> (i.e., physically reduce the bias between the SULR<sub>dir</sub> and SULR<sub>hem</sub>), since the SULR is both theoretically defined (see Eq. (1)) and practically measured (with pyrgeometer) as a hemispherically integrated value.

The following methodology contains three subsections: section 2.1

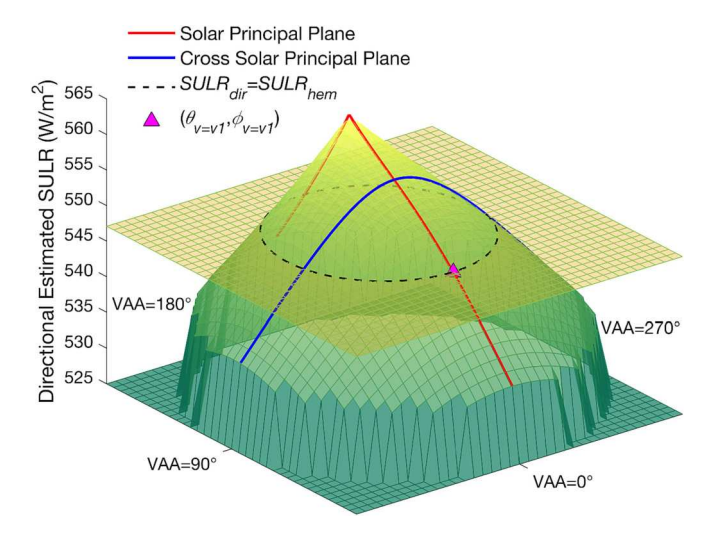


**Fig. 1.** Illustration of the  $SULR_{dir}$ ,  $SULR_{hem}$ . SPP, CSPP, and a specific viewing direction  $(\theta_{v=v1}, \phi_{v=v1})$  in the SPP (opposite side of the solar direction) with a  $SULR_{dir}$  equal to  $SULR_{hem}$ .

describes the derivation of the six-parameter time-evolving KDM; section 2.2 presents the constraints on the six parameters in the estimation based on the prior knowledge of TRD phenomenon; section 2.3 introduces the TRD correction process using the estimated parameters of the time-evolving KDM.

#### 2.1. Time-evolving KDM for single-angle estimated SULR

TIR KDMs were successfully used to simulate the angular dependence of several surface quantities, such as the bottom-of-atmosphere (BOA) DBT (Ren et al., 2014; Cao et al., 2019b), BOA directional narrowband radiance (Hu et al., 2016b) and BOA directional broadband radiance in 4–100  $\mu$ m (Hu et al., 2017).  $SULR_{dir}$  can also be an input into the KDM to simulate the angular dependence since it is the product of the BOA directional broadband radiance and  $\pi$  under the assumption of thermal isotropy (Qin et al., 2020). In the satellite scale, the hybrid method (Wang et al., 2009) was widely used to generate  $SULR_{dir}$  products with top-of-atmosphere (TOA) radiances as inputs. More details on the hybrid method for generating GOES ABI  $SULR_{dir}$  are given in Appendix I.

$$K_{Emissivity}(\theta_{v}) = 1 - \cos\theta_{v}$$
 (4)

$$K_{Chen}(\theta_s, \varphi_s, \theta_v, \varphi_v, B) = e^{\frac{-\zeta(\theta_s, \varphi_s, \theta_v, \varphi_v)}{\pi \cdot B}}$$
 (5)

$$\xi(\theta_s, \varphi_s, \theta_v, \varphi_v) = \arccos(\cos\theta_v \cdot \cos\theta_s + \sin\theta_v \cdot \sin\theta_s \cdot \cos(\varphi_v - \varphi_s))$$
 (6)

where  $\theta_s$  and  $\varphi_s$  are the SZA, SAA, respectively;  $f_{iso}$ ,  $f_{Emissivity}$  and  $f_{Chen}$  are the coefficients of the isotropic, emissivity ( $K_{Emissivity}$ , i.e., base shape kernel) and Chen ( $K_{Chen}$ , i.e., hotspot kernel) kernels, which are related to the component temperature distribution; The hotspot width B is a structure-dependent variable which needs to be calibrated (a larger B leads to a wider hotspot, details can be found in Fig. 2(d) and Fig. 17(d) in Cao et al. (2021));  $\xi$  is the angular distance between the illumination and viewing directions.

To introduce the  $SULR_{hem}$  (i.e., the target of TRD correction, it can be directly measured by the in situ pyrgeometer) into the time-evolving KDM, we assume there exists a specific viewing direction  $(\theta_{\nu=\nu 1}, \phi_{\nu=\nu 1})$  in the SPP (see the magenta triangle in Fig. 1), where  $SULR_{dir}(\theta_s, \phi_s, \theta_{\nu=\nu 1}, \phi_{\nu=\nu 1})$  is exactly equal to  $SULR_{hem}$ . Then, the  $SULR_{hem}$  can be calculated using the Vinnikov-Chen model and the specific viewing geometry as shown Eq. (7):

$$SULR_{hem} = f_{iso} + f_{Emissivity} \cdot K_{Emissivity} (\theta_{v=v1}) + f_{Chen} \cdot K_{Chen} (\theta_s, \varphi_s, \theta_{v=v1}, \varphi_{v=v1}, B)$$
(7)

Next, the difference between  $SULR_{dir}(\theta_s,\,\varphi_s,\,\theta_{\nu},\,\varphi_{\nu})$  and  $SULR_{hem}$  can be obtained:

$$SULR_{dir}(\theta_{s}, \varphi_{s}, \theta_{v}, \varphi_{v}) - SULR_{hem} = f_{Emissivity} \cdot (cos\theta_{v=v1} - cos\theta_{v})$$

$$+ f_{Chen} \cdot \left(e^{\frac{-\zeta(\theta_{s}, \varphi_{s}, \theta_{v}, \varphi_{v})}{\pi \cdot B}} - e^{\frac{-\zeta(\theta_{s}, \varphi_{s}, \theta_{v=v1}, \varphi_{v=v1})}{\pi \cdot B}}\right)$$
(8)

For the simulation of daily multi-temporal observations of a geostationary satellite, some parameters were rewritten as the function of time t, including the solar directions (i.e.,  $\theta_s(t)$  and  $\varphi_s(t)$ ), surface thermal state-related parameters (i.e.,  $SULR_{hem}(t)$ ,  $f_{Emissivity}(t)$ , and  $f_{Chen}(t)$ ) and the specific viewing directions (i.e.,  $\theta_{\nu=\nu 1}(t)$ ,  $\varphi_{\nu=\nu 1}(t)$ , see the magenta triangle in Fig. 1); some parameters remain unchanged, including the fixed viewing direction of geostationary satellite (i.e.,  $\theta_{\nu=\nu 0}$ ,  $\varphi_{\nu=\nu 0}$ ) and the hotspot width parameter that was determined by the canopy architecture (i.e., B) (Cao et al., 2021). Eq. (8) can be rewritten as:

$$SULR_{dir}(\theta_{s}(t), \varphi_{s}(t), \theta_{v=v0}, \varphi_{v=v0}) = SULR_{hem}(t) + f_{Emissivity}(t) \cdot (cos\theta_{v=v1}(t) - cos\theta_{v=v0}) + f_{Chen}(t) \cdot \left(e^{-\frac{\varepsilon(\theta_{s}(t), \varphi_{s}(t), \theta_{v=v1}(t), \varphi_{v=v1}(t), \varphi_{v=v$$

In recent, Cao et al. (2021) proposed a general framework of TIR KDM by reconsidering the physical difference between the TIR (i.e., emission) and VNIR (i.e., reflection) domains. It contains four parameters with three kernel coefficients (i.e., isotropic kernel coefficient, base shape kernel coefficient, and hotspot kernel coefficient) and an adjustable hotspot width. Four KDMs with  $R^2 > 0.940$  were designed according to this general framework. Here, the Vinnikov-Chen model among them was chosen as the basis to derive the time-evolving KDM for correcting the TRD effect of  $SULR_{dir}$ , since it has the simplest expression as given in Eqs. (3-6).

$$SULR_{dir}(\theta_{s}, \varphi_{s}, \theta_{v}, \varphi_{v}) = f_{iso} + f_{Emissivity} \cdot K_{Emissivity}(\theta_{v}) + f_{Chen} \cdot K_{Chen}(\theta_{s}, \varphi_{s}, \theta_{v}, \varphi_{v}, B)$$
(3)

The Eq. 9 could be further simplified based on the current understandings of kernels and kernel coefficients. Firstly, the  $SULR_{hem}(t)$  is parameterized as a four-parameter DVM (i.e., diurnal variation model) with the equation of  $SULR_{hem}(t) = SULR_0 + SULR_a \cdot \cos(\pi/\omega_{DVM} \cdot (t-t_m))$ , which is referenced to the daytime diurnal temperature cycle (DTC) models of LST (Duan et al., 2012). The  $SULR_0$ ,  $SULR_a$ ,  $\omega_{DVM}$  and  $t_m$  are unknown parameters to be estimated. The detailed rationale of modeling SULR DVM with the same formatted equation of LST DTC could be found in Appendix II. Secondly, the  $f_{Emissivity}(t)$  (i.e., the influence of vegetation and soil component mean temperature difference (Cao et al., 2021)) is ignored according to the approach adopted by Lagouarde and Irvine (2008) and Liu et al. (2020c). Then, the  $f_{Chen}(t)$  (i. e., the influence of sunlit and shaded mean temperature difference (Cao

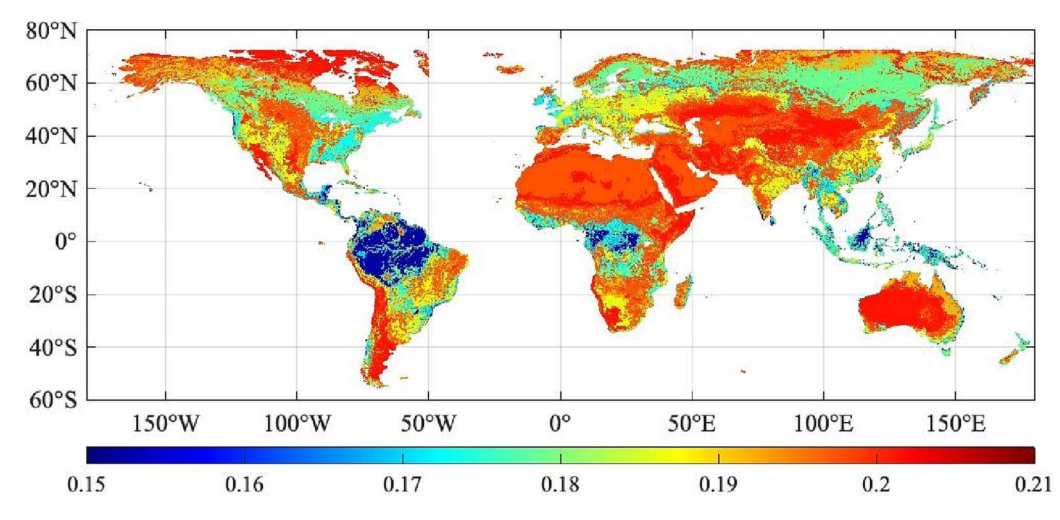


Fig. 2. Global map of the B parameter generated from the global k map.

et al., 2021)) is parameterized as  $f_{Chen}(t) = A \bullet SULR_{hem}(t) \bullet cos\theta_s(t)$  (A is an unknown parameter to be calibrated) referenced to the approach adopted by Vinnikov et al. (2012) and Wang et al. (2020), which is expected to be changed with the incoming solar radiation and surface thermal condition. Finally, the term  $e^{-\frac{1}{2}(\theta_s(t),\phi_s(t),\theta_{s-l-1}(t),\phi_{v-l-1}(t))}$  (i.e.,  $K_{Chen}$  in the direction of  $\theta_{\nu=\nu 1},\phi_{\nu=\nu 1}$ ) was ignored based on the shape of  $K_{Chen}$  (it declines quickly when viewing direction is away from the solar direction (Lagouarde and Irvine, 2008; Cao et al., 2021)) and the specific location of  $(\theta_{\nu=\nu 1},\phi_{\nu=\nu 1})$  (it locates in the opposite side of solar direction in the SPP plane, see Fig. 1). A six-parameter time-evolving KDM can be obtained after the four steps previously introduced (see Eq. 10 below).

$$\begin{split} SULR_{dir}(\theta_{s}(t),\varphi_{s}(t),\theta_{v=v0},\varphi_{v=v0}) &= \left(SULR_{0} + SULR_{a} \cdot cos\left(\frac{\pi}{\omega_{DVM}}(t-t_{m})\right)\right) + \\ &A \cdot \left(SULR_{0} + SULR_{a} \cdot cos\left(\frac{\pi}{\omega_{DVM}}(t-t_{m})\right)\right) \cdot cos\theta_{s}(t) \cdot e^{\frac{-\varepsilon(\theta_{s}(t),\varphi_{s}(t),\theta_{v=v0},\varphi_{v=v0})}{\pi \cdot B}} \\ &, t_{sr} \leq t \leq t_{ss} \end{split}$$

$$(10)$$

where  $SULR_{dir}$  and  $SULR_{hem}$  are the directional SULR and the hemispherically integrated SULR, respectively; t denotes the local time;  $\theta_s(t)$  and  $\varphi_s(t)$  are the temporally varied SZA and SAA, respectively;  $\theta_{v=v0}$  and  $\varphi_{v=v0}$  are the fixed VZA and VAA for a specific geolocation of geostationary satellite;  $\xi(\theta_s(t), \varphi_s(t), \theta_{v=v0}, \varphi_{v=v0})$  is the angular distance between temporally varied solar geometry and the fixed viewing direction of geostationary satellite. The A and B are unknown parameters that indicating the hotspot amplitude and hotspot width, respectively; the  $SULR_0$ ,  $SULR_a$ ,  $\omega_{DVM}$  and  $t_m$  are the unknown parameters that indicating the residual SULR near sunrise ( $t_{sr}$ ), the SULR amplitude, the half-period parameter and the time at the SULR maximum, respectively. The  $t_{ss}$  is the time near sunset. The  $t_{sr}$  and  $t_{ss}$  are easy to determine given the geolocation and date (Sinnott, 1994). The six parameters of the time-evolving KDM (i.e.,  $SULR_0$ ,  $SULR_a$ ,  $\omega_{DVM}$ ,  $t_m$ , A, B) could be calibrated with not less than six clear sky directional observations.

The half-period parameter of LST DTC model (i.e.,  $\omega_{DTC}$ ) can be calculated using geolocation and date (Göttsche and Olesen, 2001; Duan et al., 2012). The half-period parameter of DVM model (i.e.,  $\omega_{DVM}$ ) is related to the  $\omega_{DTC}$  because the SULR is the 4th power of LST. However, there exists an offset between  $\omega_{DVM}$  and  $\omega_{DTC}$ . We found  $\omega_{DVM}$ - $\omega_{DTC} \in [-3.8, -0.2]$  with 36,300 groups of synthetic datasets. The  $\omega_{DTC}$  calculation using geolocation and date and the boundary determination of  $\omega_{DVM}$ - $\omega_{DTC}$  using synthetic dataset could be found in Appendix III.

Finally, we obtained a six-parameter time-evolving KDM (including  $SULR_0$ ,  $SULR_a$ ,  $\omega_{DVM}$ ,  $t_m$ , A, B) to correct the TRD effect of geostationary satellite SULR datasets by conducting temporal extension to the original

TIR KDM. This proposed time-evolving KDM was composed of a four-parameter SULR DVM and a two-parameter TRD amplitude model. The six parameters of the time-evolving KDM can be regressed using not less than six clear-sky daytime observations and then the  $SULR_{dir}$  can be easily corrected to  $SULR_{hem}$ .

#### 2.2. Constraints on the KDM parameters

Physically-based initial guesses and ranges of the six parameters of the time-evolving KDM determine the quality of the retrieved parameters using the least square regression. Here, the widely-used "trust-region-reflective" algorithm (Li and Coleman, 1994; Coleman and Li, 1996) integrated in the MATLAB platform was adopted. For the  $\omega_{DVM}$ , the initial value was set as  $\omega_{DTC}$ -2 and the boundary was set as  $[\omega_{DTC}$  -3.8,  $\omega_{DTC}$  – 0.2] (more details could be found in Appendix III). For the another three DVM parameters, the regressed corresponding DVM parameters based on multi-temporal  $SULR_{dir}$  (i.e.,  $SULR_0$ ,  $SULR_a$ , and  $t_m$ ) were used as the initial values of the unknown DVM parameters of  $SULR_{hem}$  (i.e.,  $SULR_0$ ,  $SULR_a$ , and  $t_m$ ). Then, the boundaries of  $SULR_0$ ,  $SULR_a$ , and  $t_m$  were set as  $[SULR_0'-80, SULR_0'+80]$ ,  $[SULR_a'-80, SULR_a'+80]$ 80] and  $[t_m'-2,t_m'+2]$ , respectively, considering that the bias of absolute SULR values is usually  $< 80 \text{ W/m}^2$  and the bias of time is always < 2 h. Parameter A in Eq. (10) indicates the maximum TRD amplitude. Its initial value (A') was set to 0.05 with boundaries of [0, 0.1]. This parameter relies on a reasonable assumption: the maximum TRD amplitude is usually <10% of SULR (Hu et al., 2016b). Parameter B in Eq. (10) is a structure-dependent hotspot width. Ermida et al. (2018) generated the global hotspot width k values of Vinnikov-RL KDM through clustering the surface characteristics. Cao et al. (2021) built the relationship between the hotspot width B of Vinnikov-Chen KDM and the hotspot width *k* of the Vinnikov-RL KDM. Fig. 2 below shows the *B* value distribution computed from the global k map (personal communication). The B value in Fig. 2 was set as the initial value (B') with boundaries of  $[0.5 \cdot B', 1.5 \cdot B']$ . The initial values and boundaries of the all

**Table 1**Initial values and boundaries of the six parameters of the time-evolving KDM.

Parameter	Initial value	Boundaries
SULR <sub>0</sub>	SULR <sub>0</sub>	[SULR <sub>0</sub> ' - 80, SULR <sub>0</sub> ' + 80]
$SULR_a$	$SULR_a$	$[SULR_a - 80, SULR_a + 80]$
$\omega_{DVM}$	$\omega_{DTC}$ –2	$[\omega_{DTC}-3.8, \omega_{DTC}-0.2]$
$t_m$	$t_m$	$[t_m'-2,t_m'+2]$
A	A'	[0, 0.1]
В	B'	$[0.5 \cdot B', 1.5 \cdot B']$

six parameters are listed in Table 1.

## 2.3. TRD correction with the regressed six parameters of the time-evolving KDM

Multi-temporal observations of geostationary satellite make the six-parameter of the time-evolving KDM (i.e., Eq. 10) solvable. The TRD-corrected SULR ( $SULR_{hem}$ ) at a specific daytime hour  $t_0$  can be directly calculated with Eq. (11) once the four DVM parameters of  $SULR_{hem}$  (i.e.,  $SULR_0$ ,  $SULR_0$ ,  $SULR_0$ , DVM, and  $t_m$ ) are calibrated.

$$SULR_{hem} = SULR_0 + SULR_a \cdot cos\left(\frac{\pi}{\omega_{DVM}}(t_0 - t_m)\right)$$
(11)

The SULR accuracy before and after applying the TRD correction can be quantified by the RMSE and mean bias error (MBE) taking in situ measured  $SULR_{hem}$  as a reference (Eqs. (12) and (13)).

$$RMSE = \sqrt{\frac{\sum_{i=1}^{N} \left(SULR_i - SULR_{hem,i}\right)^2}{N}}$$
 (12)

$$MBE = \frac{1}{N} \sum_{i=1}^{N} \left( SULR_i - SULR_{hem,i} \right)$$
 (13)

where N is the number of clear-sky observation samples,  $SULR_i$  is the estimated SULR before ( $SULR_{dir,i}$ ) or after ( $SULR_{hem,i}$ ) TRD correction for the  $i^{th}$  sample, and  $SULR_{hem,i}$  is the hemispherically integrated true value of  $SULR_{hem}$  for the  $i^{th}$  observation (e.g., the in situ measured result).

# 3. Validation and sensitivity analysis of the time-evolving KDM based on a DART-simulated dataset

### 3.1. Validation and sensitivity analysis strategy

Before being used in the satellite observations, the KDMs are usually validated using a simulated dataset generated by 3D physically-based models (Wang et al., 2018; Cao et al., 2019a; Jiang et al., 2021), such as the widely-used Discrete Anisotropic Radiative Transfer (DART) model. The DART model is one of the most comprehensive and accurate 3D models to simulate the radiative budget and satellite observations of land surfaces in the visible, near infrared, and TIR spectral regions (Gastellu-Etchegorry et al., 2012; Gastellu-Etchegorry et al., 2015; Wang et al., 2022). It is powerful to realistically describe vegetation and urban landscapes, which makes it suitable to cross-validate analytical and

parametric models (Pinheiro et al., 2006; Cao et al., 2018; Wang et al., 2018; Cao et al., 2019a). The time-evolving KDM proposed in section 2 was validated with a dataset issued from DART mock-up. Fig. 3 shows the detailed flowchart of the validation and sensitivity analysis process of the time-evolving KDM using the DART-simulated dataset. The validation and sensitivity analysis strategy were presented in section 3.1. The DART-simulated dataset was introduced in section 3.2. Finally, the validation and sensitivity results were given in section 3.3 and section 3.4, respectively.

DART was run with the scene description parameters as inputs, for example, the numbers of trees adapted with the leaf cover fraction, the geolocations related to the satellite viewing angles, the dates and times that determine the solar illumination angles, the temperatures and emissivities of each component, and finally the wavelengths that describe the spectral ranges of interest. Section 3.2 describes the DART input parameters, the SULR integration process, and the simulated dataset. The DART-simulated daily multi-temporal SULR<sub>dir</sub> values of a geostationary satellite, viewing and illumination geometry values, and corresponding imaging times formed inputs of the 6-parameter timeevolving KDM (i.e., Eq. 10) to calibrate the parameters. Then, the KDM-fitted SULR<sub>dir</sub> using the calibrated 6 parameters will be evaluated against the DART-simulated SULR<sub>dir</sub> values. Section 3.3 presents the validation results of the proposed time-evolving KDM in modeling directional SULR values at different situations. Section 3.4 conducts the sensitivity analysis with different numbers of inputs and temporal combinations to further study the performance of time-evolving KDM at different observation conditions.

### 3.2. DART-simulated dataset

As shown in Fig. 4, we synthesized nine 90 m  $\times$  90 m forest scenes to study the impact of scene structure on the TRD effect, named Scene 1–9, respectively. The forest scenes consist of three crown shapes (spherical, ellipsoidal, and cylindrical shape with a conical top (i.e., cone-cylinder) (Chen and Leblanc, 1997)) and three leaf area index (LAI) values (LAI = 1 with 83 trees, LAI = 2 with 187 trees and LAI = 4 with 342 trees). For each scene, three typical leaf angle distributions (LADs, i.e., spherical, planophile and erectophile (Chen and Black, 1991)) were considered. The trunks and tree crowns are simulated with facets in DART and the directional radiance are generated using the DART-Lux mode (Wang and Gastellu-Etchegorry, 2021; Wang et al., 2022). The emissivity spectra of the scene elements are obtained from the DART optical database: "loam gravelly brown dark" for the soil, "leaf deciduous" for the leaves, and "bark deciduous" for the trunks.

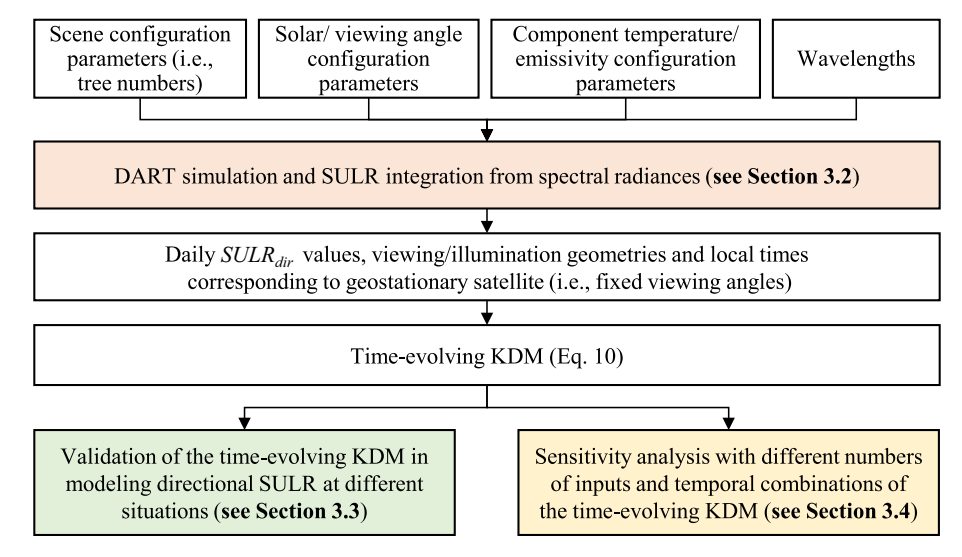
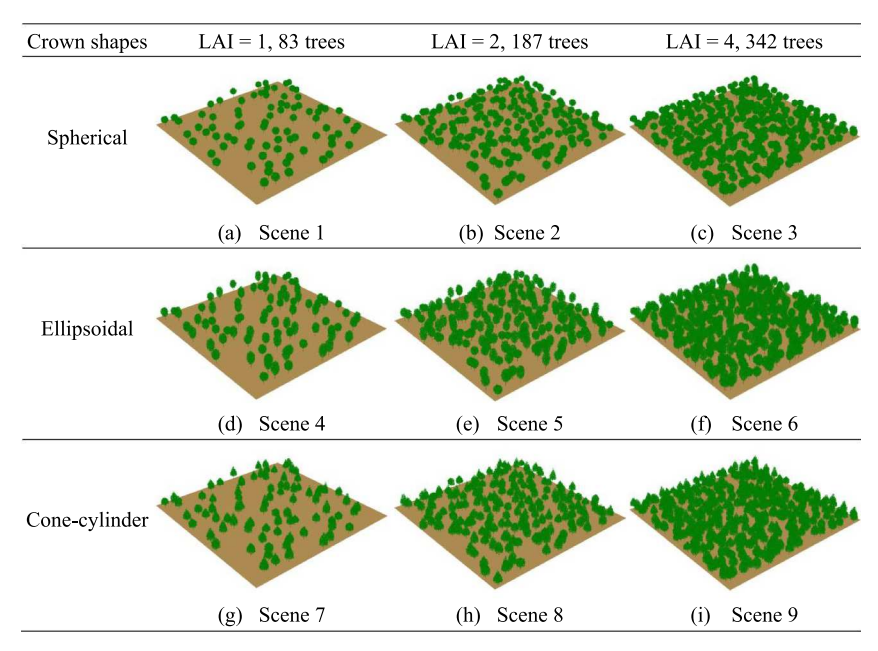


Fig. 3. Flowchart of the validation and sensitivity analysis of the time-evolving KDM using the DART-simulated dataset.



**Fig. 4.** DART-simulated forest scenes. (a-i) Scenes 1–9. The trees in spherical forest scenes (Scenes 1–3) are identical which have the same tree height (6 m) with 2 m radius tree crown and 2 m trunk height below the crown; while the trees in ellipsoidal and cone-cylinder forest scenes (Scenes 4–6 and Scenes 7–9) are different which have tree heights ranging 4 m - 8 m (6 m on average in each scene) with 2 m trunk height below the crown. The semiminor axis of the spheroid and the radius of the cylinder are both equal to the radius of the spherical crown (2 m). The trunk diameters of all trees are 0.1 m.

Besides the scene structure description parameters, DART also needs the input of component temperatures to simulate the canopy DBT patterns. DART calculates the 3D temperature  $T_{i,j}$  of scene element j of  $i^{th}$  component (e.g., leaves) by assuming that the temperature of element j

increases with increasing illumination (i.e.,  $T_{i,j}$  depends on the solar illumination of element j). Accordingly, DART first simulates the solar illumination of the scene and then determines the  $T_{i,j}$  using a predefined temperature property of the mean temperature  $\overline{T}_i$  (i.e.,  $0.5 \cdot (T_{i,\max} + T_{i,j})$ ).

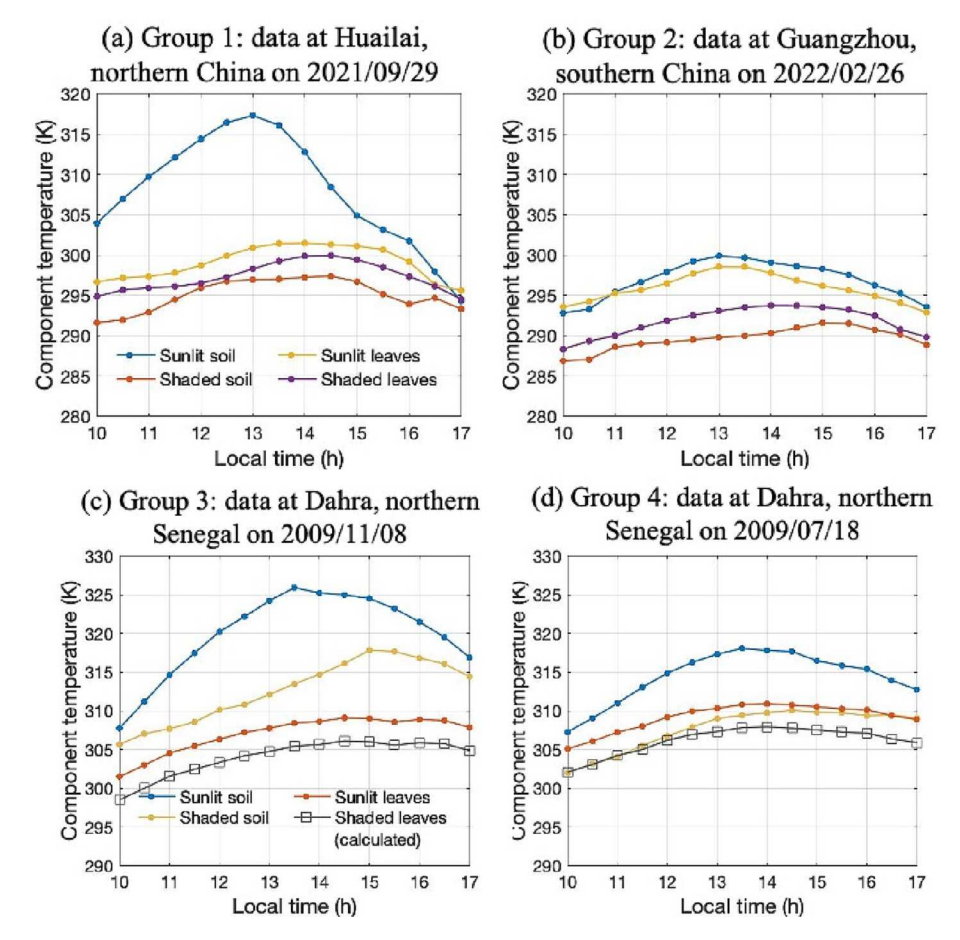
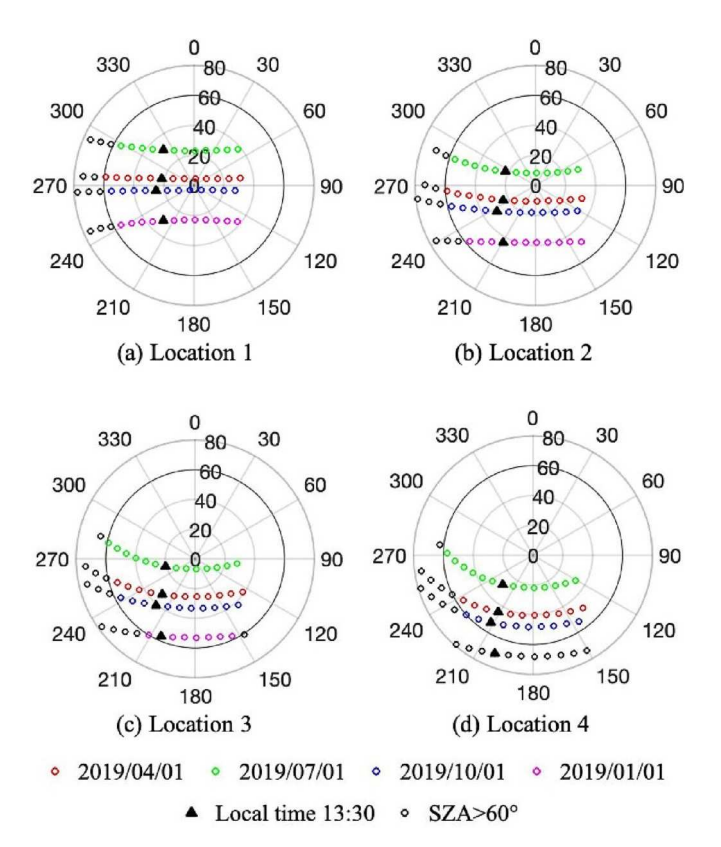


Fig. 5. Four groups of component temperatures acquired at different dates and locations. (a-b) Measured four component temperatures at Huailai, northern China on 2021/09/29 and at Guangzhou, southern China on 2022/02/26, respectively; (c-d) Measured/calculated component temperatures at Dahra, northern Senegal on 2009/11/08 and 2009/07/18, respectively.

min)) and temperature range  $\Delta T_i$  (i.e.,  $T_{i,max}$ - $T_{i,min}$ ) for type i (i.e.,  $T_{i,j} \in T_{i,j}$  $[T_{i,min}, T_{i,max}]$ ). Here, each scene has two types of elements: vegetation (i. e., leaves and trunks) and background (i.e., soil). To ensure the reliability of DART simulations, we used four groups of in situ measured clear-sky diurnal cycles of temperature components at different locations and dates, including one group measured at Huailai (northern China, geolocation: 40.349695°N, 115.7944417°E) on 2021/09/29, one group measured at Guangzhou (southern China, geolocation: 23.06310278°N, 113.3961633°E) on 2022/02/26, and two groups of data measured at Dahra (northern Senegal, geolocation: 15.402°N, 15.443°W) on 2009/11/08 and 2009/07/18. The two groups of four component temperatures (i.e. sunlit/shaded soil and sunlit/shaded leaf) acquired in China were measured by handheld "Fluke 561" thermometer, while the another two groups in Dahra were measured by towerbased "KT-15.85 IIP" TIR radiometers (self-calibrating chopped radiometers, Heitronics GmbH) (Rasmussen et al., 2011). The temperature of shaded leaves was not measured in Dahra because of the technical difficulty in measurement with tower-based instruments (Rasmussen et al., 2011). Here, we assumed that the temperature difference between sunlit and shaded leaves is 3 K based on the analysis of another two groups of in situ datasets measured in China. Fig. 5 shows the measured/ calculated temperature values of the four components.

The geolocations of the scenes and the imaging dates and times need to be predefined to determine the illumination directions. Here, we defined four sites in different geolocations: Location 1 (0°N, 0°E), Location 2 (15°N, 0°E), Location 3 (30°N, 0°E), and Location 4 (45°N, 0°E), and four typical dates in 2019: 2019/04/01 (spring), 2019/07/01 (summer), 2019/10/01 (autumn), and 2019/01/01 (winter). The solar direction (Fig. 6) was simulated every 30 min for each day in the period of 10:00-17:00 to achieve the high-frequency observation of geostationary satellite. The situations with SZA>60° (i.e., black circles in



**Fig. 6.** Polar plots of the illumination angles on 2019/04/01 (spring), 2019/07/01 (summer), 2019/10/01 (autumn), and 2019/01/01 (winter) for the four sites: (a) Location 1 (0°N, 0°E) and (b) Location 2 (15°N, 0°E); (c) Location 3 (30°N, 0°E); (d) Location 4 (45°N, 0°E). The concentric circles and radial lines indicate the solar zenith angles and solar azimuth angles, respectively.

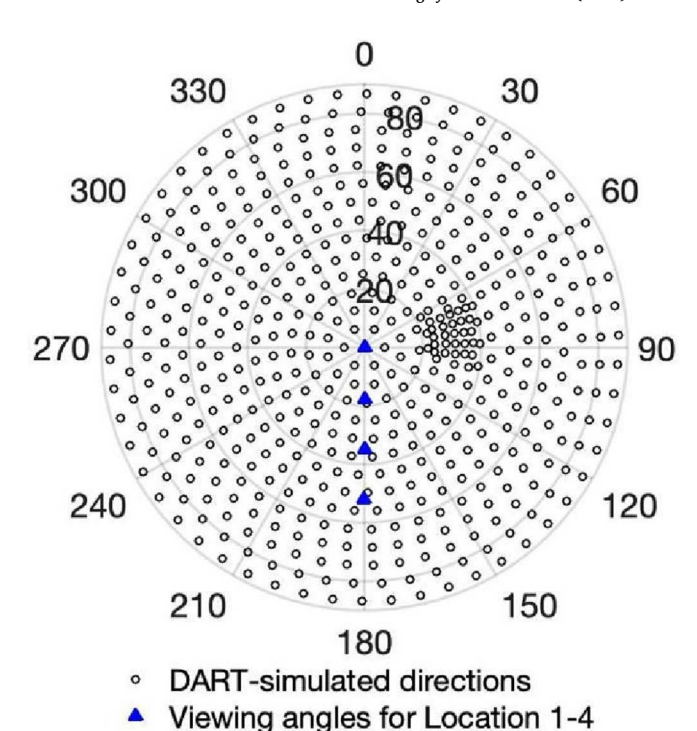


**Fig. 7.** Polar plots of viewing angles for the four sites and 530 discrete DART-simulated directions in the upper hemisphere for 2019/04/01 10:00 for Location 1. The concentric circles and radial lines indicate the viewing zenith angles and viewing azimuth angles, respectively.

Fig. 6) were not considered due to the relatively weak TRD effect for the late afternoon. The temporal changes in the solar direction differ markedly on these four days as shown in Fig. 6, showing 8–14 available observations except the winter day of Location 4 (see Fig. 6(d)).

We considered a geostationary satellite with a subpoint located at latitude =  $0^{\circ}$  and longitude =  $0^{\circ}$  that observes the predefined four sites. The viewing angles (VZA, VAA) are  $(0^{\circ}, 180^{\circ})$ ,  $(17.62^{\circ}, 180^{\circ})$ ,  $(34.96^{\circ}, 180^{\circ})$ , and  $(51.82^{\circ}, 180^{\circ})$  for Location 1–4, respectively. Location 1 (2–4) was selected to study the TRD influence of nadir (oblique) viewing direction on the estimated SULR. The polar plots of viewing angles of this virtual geostationary satellite for the four sites were plotted in Fig. 7 (see blue triangles). DART was run with 500 directions in the lower hemisphere and 530 directions in the upper hemisphere (including 30 additional directions in the hot spot region). Fig. 7 shows an example of the 530 discrete DART-simulated directions in the upper hemisphere for  $2019/04/01\ 10:00$  for Location 1.

To obtain accurate SULR values when integrating spectral radiance, the interval 4–100  $\mu m$  was sampled with 66 narrow bands in DART simulations. Bands 1–40 locate in 4–14  $\mu m$  interval with  $\Delta\lambda=0.25$   $\mu m$ , bands 41–51 were set in 14–25  $\mu m$  with  $\Delta\lambda=1$   $\mu m$  and bands 52–66 were set in 25–100  $\mu m$  with  $\Delta\lambda=5$   $\mu m$ . The directional spectral radiance was simulated using DART, and then the  $SULR_{dir},~SULR_{hem},~$  and TRD were calculated using Eqs. (14-16).

$$SULR_{dir}(\Omega_{j}) = \pi \cdot \sum_{i=1}^{66} L_{dart}(\lambda_{i}, \Omega_{j}) \cdot \Delta \lambda_{i}$$
 (14)

$$SULR_{hem} = \sum_{j=1}^{530} \frac{SULR_{dir}(\Omega_j)}{\pi} \cdot cos\theta_j \cdot \Delta\Omega_j$$
 (15)

$$TRD = SULR_{dir} - SULR_{hem} \tag{16}$$

where  $L_{dart}(\lambda_i, \Omega_j)$  is the DART-simulated ground-leaving radiance of the scene (including the surface emitted radiance and the reflected atmosphere downwelling longwave radiance) for the spectral band  $(\lambda_i, \Delta \lambda_i)$ , i  $\in [1, 66]$ , for the upward discrete direction  $\Omega_i$  with  $j \in [1, 530]$  and  $\theta_i$  is

Table 2
Summary of the main input parameters of DART.

Parameter	Value	Parameter	Value
Scene area	90 m × 90 m	Leaf angle distribution	Spherical, planophile, and erectophile
Cell size	$\begin{array}{l} 0.5\times0.5\times0.5\\ m^3 \end{array}$	Crown shape	Spherical, ellipsoidal and cone-cylinder crown shapes
Number of directions	1030	Soil emissivity	loam_gravelly_brown_dark
Wavelength	66 bands in 4–100 μm	Trunk emissivity	bark_deciduous
Number of trees	[83, 187, 342]	Leaf emissivity	leaf_deciduous
LAI	[1.0, 2.0, 4.0]	Geolocation	(0°N, 0°E), (15°N, 0°E), (30°N, 0°E), and (45°N, 0°E)
Tree height	6 m for spherical crown shape, 4–8 m for ellipsoidal and cone-cylinder crown shape	$\overline{T}$ and $\Delta T$	See Fig. 5
Trunk height below the crown	2 m	Date	2019/04/01, 2019/07/01, 2019/10/01, and 2019/01/ 01
Trunk diameter	10 cm	Time	Restricted to 10:00–17:00 (30-min step) and SZA $\leq$ 60 $^{\circ}$
Atmosphere brightness temperature	260 K		

the zenith angle of direction  $\Omega_j$ . The atmosphere brightness temperature is set as the default value of 260 K in the simulations. See Appendix IV for the sensitivity analysis of SULR to atmosphere downwelling longwave radiation (DLR) variation in one day.

Table 2 summarizes the main input parameters used in the DART simulation. It can be found that a total of 19,224 simulations were carried out with 9 scenes, 3 LADs, 4 groups of component temperatures, 4 locations, 4 dates, and 8–14 measurements per day. The numbers of DART-simulated data points at different local times are shown in Fig. 8. Because of the restriction of SZA $\leq$ 60°, a relatively small numbers of data points are obtained in the morning (10:00) and late afternoon (14:30–16:30).

#### 3.3. Validation results with the DART-simulated dataset

The value of B' (initial guess for B) is required for each scene in the fitting of  $SULR_{dir}$ , as described in section 2.2. However, B value in Fig. 2 was not suitable here since the scenes were manually constructed in DART (i.e., no specific geographic location). The configurations of the trees in this study (Scenes 1–3, 4–6, and 7–9) were the same as the scenes D, E, and F of Cao et al. (2021). Hence, B values were calculated using the simulated multiangle DBTs in their work. The B values (0.15, 0.13, and 0.10 for Scene 1/4/7, 2/5/8, and 3/6/9) were directly set as the initial values (B'). Using the DART-simulated daily multitemporal  $SULR_{dir}$  values, the corresponding viewing/illumination directions and time t, the six unknowns of the time-evolving KDM can be calibrated and then the modeled  $SULR_{dir}$  values can be calculated. Scatterplot between the DART-simulated  $SULR_{dir}$  and time-evolving KDM modeled  $SULR_{dir}$  with all simulation dataset and the related histogram of the modeling

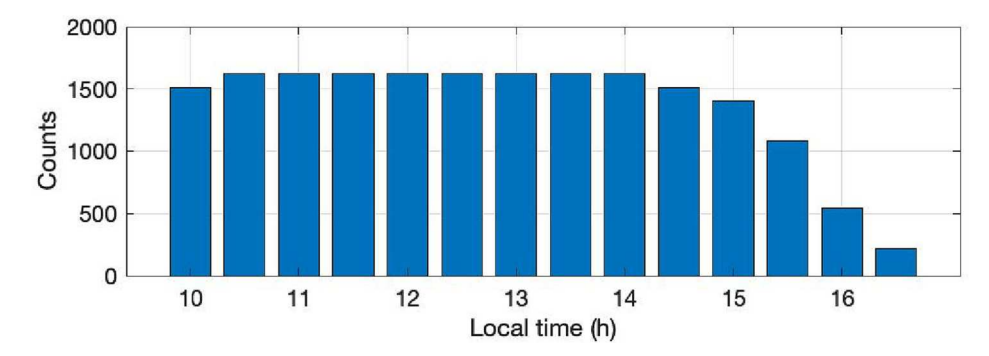


Fig. 8. The count distribution of 19,224 DART simulations at different local times.

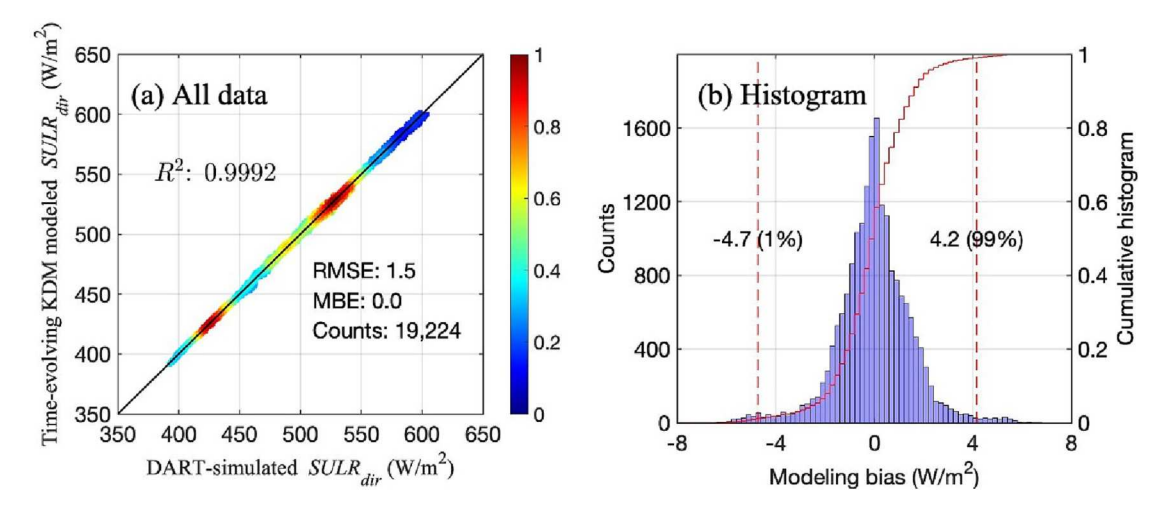


Fig. 9. Scatterplot between DART-simulated  $SULR_{dir}$  and time-evolving KDM modeled  $SULR_{dir}$  with all simulation dataset (a) and the related histogram of the modeling bias (b).

bias are plotted in Fig. 9a and Fig. 9b, respectively.

Fig. 9a demonstrates that the simulated  $SULR_{dir}$  dataset covers a wide range of values from 392.0 W/m² to 604.0 W/m². The time-evolving KDM can model the daily multi-temporal  $SULR_{dir}$  values with an R² = 0.9992, an RMSE of 1.5 W/m² and an MBE of 0.0 W/m², which shows a good fitting ability of the time-evolving KDM. The RMSE of time-evolving KDM is comparable to that of the single temporal Vinnikov-Chen KDM (i.e., 0.21 K) (Cao et al., 2021), noting that a LST bias of 1 K is equivalent to a SULR bias of 6 W/m² when LST around 300 K. Fig. 9b shows the histogram of the modeling bias, indicating 98% of the bias ranges in [-4.7, 4.2] W/m² (taking the cumulative histogram of 1% and 99% as two thresholds). The relatively symmetric distribution of modeling bias explains the situation of MBE = 0.0 W/m² in Fig. 9a.

The performance of the time-evolving KDM at different LAIs, crown shapes and LADs were given in Fig. 10a. All of the nine RMSEs were within 2 W/m², which shows the acceptable modeling accuracy of the time-evolving KDM. The RMSEs of different LAI values have a relatively larger range from 1.0 W/m² (LAI = 4) to 2.0 W/m² (LAI = 1). The time-evolving KDM has a much more stable performance for different crown shapes and LADs with an RMSE from 1.4 W/m² to 1.5 W/m². Fig. 10b shows that the time-evolving KDM has an RMSE fluctuation between 1.0 W/m² and 2.1 W/m² at different local times. The maximum RMSE of 2.1 W/m² at local time 13:30 is close to that of LAI = 1 in Fig. 10a (2.0 W/m²). Therefore, the new 6-parameter time-evolving KDM has an acceptable modeling accuracy for different LAIs, crown shapes, LADs and local times.

## 3.4. Sensitivity analysis of the time-evolving KDM with different numbers of inputs and temporal combinations

All available observations with SZA  $\leq 60^\circ$  were used to drive the time-evolving KDM in the section 3.3, however, not all observations are available due to the existence of clouds in reality. Therefore, it is important to study the performance of the time-evolving KDM with different numbers of inputs and different temporal combinations. Here, the observations of Location 1 at 10:00–15:30 (see Fig. 6a; 12 observations per day) of all 48 days (4 typical days \*3 scenes with spherical crown shapes and spherical LAD \* 4 groups of component temperatures) were adopted to perform the sensitivity analysis.

The performance of the time-evolving KDM with N inputs ( $N \in [6,12]$ ) was evaluated using  $48*N*C_{12}^N$  ( $N \in [6,12]$ ) observations. Fig. 11a shows the modeling accuracies of the time-evolving KDM with N numbers of inputs. The time-evolving KDM has a better performance with the increase of N. The overall RMSE decreases from 3.68 W/m<sup>2</sup> of N = 6 to 1.80 W/m<sup>2</sup> of N = 12. Then, we further studied the performance of the time-evolving KDM with different temporal combinations, taking N = 6

with 924 combinations as an example (i.e.,  $C_{12}^6$ =924). Each combination has 48\*6 values. Fig. 11b plots the 924 RMSEs using the average value (Avg., see y-axis below) and standard derivation (STD, see x-axis below) of each combination as axes. Results show that the combinations with larger STD (more scattered in time) and larger average SULR values (more likely around noon) have better performance (i.e., relatively lower RMSE values in blue color). In summary, the time-evolving KDM will get a better accuracy with a larger number of inputs, with temporally scattered local times and with larger average SULR values.

# 4. Validation of the TRD correction method based on ABI/GOES-16 and in situ measurements

### 4.1. Validation strategy of the TRD correction method

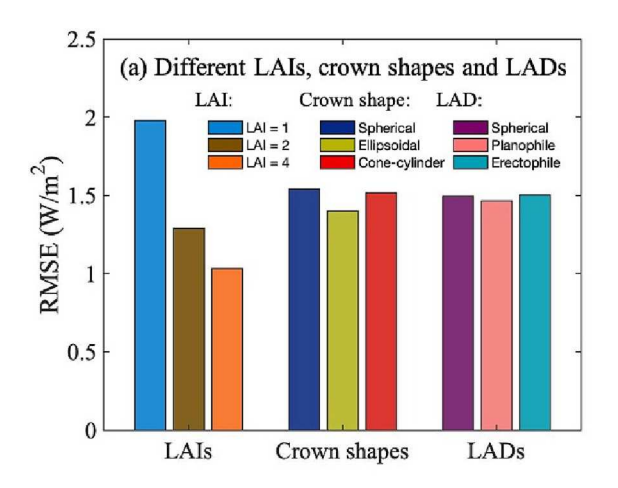
As a practical method to correct the TRD effect of SULR product of geostationary satellites, it is important to assess its performance on a specific satellite product. Here, the TRD correction method is further validated with GOES-16 ABI dataset and AmeriFlux in situ measurements. As indicated by previous studies (Minnis and Khaiyer, 2000; Coll et al., 2019), the TRD amplitude is much larger during the daytime and for heterogeneous surfaces. The TRD correction method is validated under daytime clear-sky conditions, based on ABI satellite observations and in situ SULR measurements for 20 vegetated AmeriFlux sites. The flowchart of the validation work is shown in Fig. 12.

There are three main steps in the validation of the TRD correction method with ABI/GOES-16 satellite data: (1) the clear-sky single-angle SULR was first estimated using Eq. (I.1) of the hybrid method (Wang et al., 2009) with inputs of the ABI TOA radiance in bands 11, 14 and 15 (i.e., 8.5, 11.2 and 12.3  $\mu$ m, respectively), clear-sky masks, corresponding viewing angles, and SULR estimation coefficients (see Appendix I for more details); (2) the estimated single-angle SULR, the corresponding imaging time, and corresponding viewing and illumination angles forms input of the time-evolving KDM model to get its coefficients and then implement the TRD correction (see section 2 above); (3) the proposed method is validated by comparing the TRD-corrected SULR with the in situ measured SULR. The comparison results can be found in section 4.3.

### 4.2. Data for validation

### 4.2.1. ABI data from GOES-16

GOES-16 is the first of the GOES-R satellite series. It was declared operational on December 18th, 2017. ABI instrument onboard GOES-16 is positioned at  $0^{\circ}\text{N},~75.2^{\circ}\text{W}.$  ABI includes six VNIR bands, four shortwave/mid-wave infrared bands, and six TIR bands. Its spatial



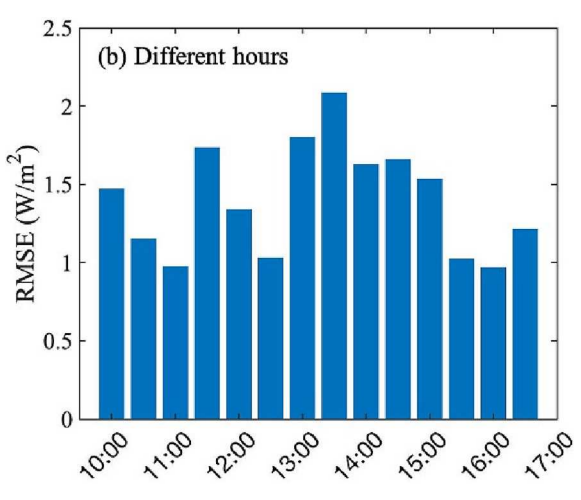


Fig. 10. Performance of the time-evolving KDM at different LAIs, crown shapes, LADs (a) and local times (b).

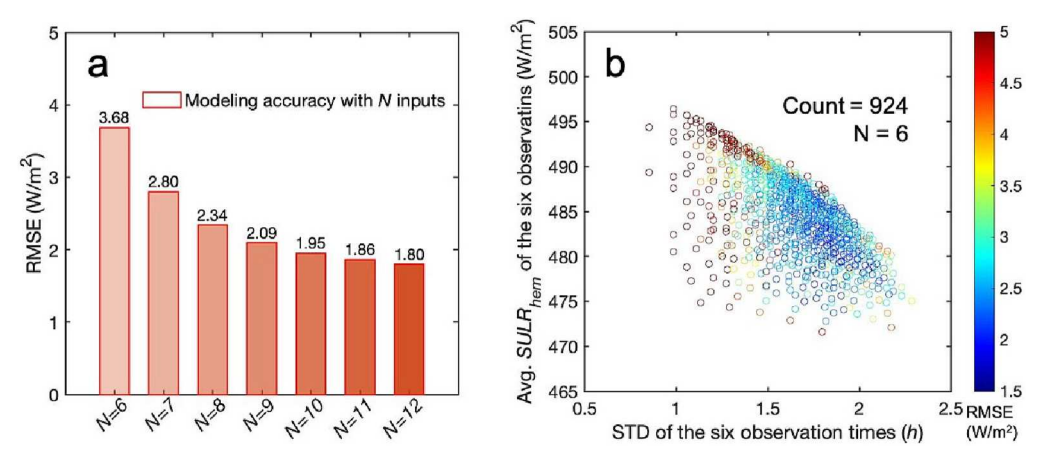
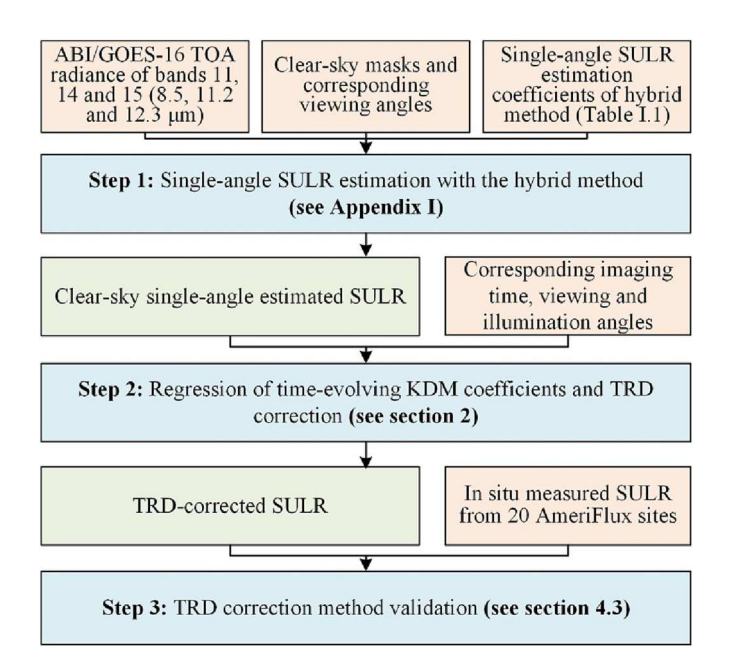


Fig. 11. The modeling accuracy of the time-evolving KDM with different number of inputs (a) and different temporal combinations (b).



 $\begin{tabular}{ll} Fig.~12. Flowchart of the validation using ABI/GOES-16 data and AmeriFlux in situ measurements. \end{tabular}$ 

resolution at the satellite subpoint is 0.5 km for one band (0.64  $\mu m), 1$  km for three bands (0.47, 0.865, 1.61  $\mu m)$ , and 2 km for the other bands, notably TIR bands. Its temporal resolution could be better than 30 min per scanning. Here, we take advantage of the highest frequency of geostationary satellite observations to validate the proposed time-evolving KDM and TRD correction method.

The TOA radiance products of ABI bands 11 (8.55  $\mu$ m), 14 (11.2  $\mu$ m), and 15 (12.3  $\mu$ m) and the cloud mask product were used to calculate the clear-sky SULR. Full disk data satisfying the filtering criteria (10:00–17:00 local time with an interval of 30 min) for 2018 and 2019 were downloaded from the national oceanic and atmospheric administration comprehensive large array-data stewardship system (http://www.class.noaa.gov/) to estimate the SULR. The downloaded dataset includes 10,950 full disk imagery in total.

### 4.2.2. AmeriFlux in situ measurement dataset

The coarse resolution of the ABI TIR bands requires a selection of validation sites having good spatial representativeness at large scale. Chu et al. (2021) classified the representativeness of 214 AmeriFlux sites as high, medium, and low homogeneity at footprint radii of 250–3000 m around flux towers by analyzing the measurement heights, underlying

land cover, ground surface characteristics, wind directions, and turbulent state of the atmosphere. At the scale of 2 km corresponding to the nadir spatial resolution of ABI TIR bands, 20 AmeriFlux sites were retained based on GOES-16/ABI disk coverage and in situ data availability in 2018–2019, which include five highly representative sites and 15 moderately representative sites.

The spatial distribution of these 20 AmeriFlux sites is plotted in Fig. 13 with the base map of 500 m-resolution MCD12Q1 2018 yearly International Geosphere Biosphere Programme (IGBP) land cover classifications (Friedl et al., 2002). The detailed information of these sites is summarized in Table 3. The 20 selected AmeriFlux sites include seven types of IGBP land covers: one site of woody savanna (WSA), three sites of open shrubland (OSH), four sites of grassland (GRA), one site of cropland (CRO), one site of mixed forest (MF), four sites of deciduous broadleaf forest (DBF), and six sites of evergreen needleleaf forest (ENF). The temporal resolutions of the downloaded in situ measured SULR were 30 min at all sites except site US-MMS. Furthermore, part of the SULR observations were missing for sites US-Kon, US-Syv, and US-Ho1, whose temporal coverages were 2018.01–2018.10, 2018.01–2018.11 & 2019.08–2019.12, and 2018.01–2018.06, respectively. The temporal coverages of the remaining sites were 2018.01–2019.12.

The in situ measurements were filtered with three criteria: local solar time of 10:00-17:00, SZA<60°, and the number of daily clear-sky halfhour observations >6. Finally, we obtained 34,220 groups of validation data, including 13,847 groups of highly representative site data and 20,373 groups of moderately representative site data. The count distributions of the validation data by site, month, and local time are plotted in Fig. 14. As shown in Fig. 14a, a sufficient number of data is available at each site to conduct a reliable validation. For instance, the number of validation data for the 5 most representative sites ranges from 1014 to 3561 with an average value of 2769. The number of available validation data points of the 15 moderately representative sites ranges from 225 to 3546 with an average value of 1358. Fig. 14b demonstrates that the count distribution of validation data by month shows an increasing trend from January to June and a decreasing trend from June to December because the SZA is relatively small in summer; therefore, more days satisfied the criterion of ≥6 clear-sky observations were selected under the restriction of SZA < 60°. Likewise, as shown in Fig. 14c, the validation data showed an increasing trend from morning to noon and a decreasing trend from noon to afternoon because the SZA at noon is relatively small, while the SZA in the early morning and late afternoon is more likely to be excluded. There were adequate numbers of data points among the highly and moderately representative sites in different months and local times, as shown in the two kinds of color in Fig. 14b-c.

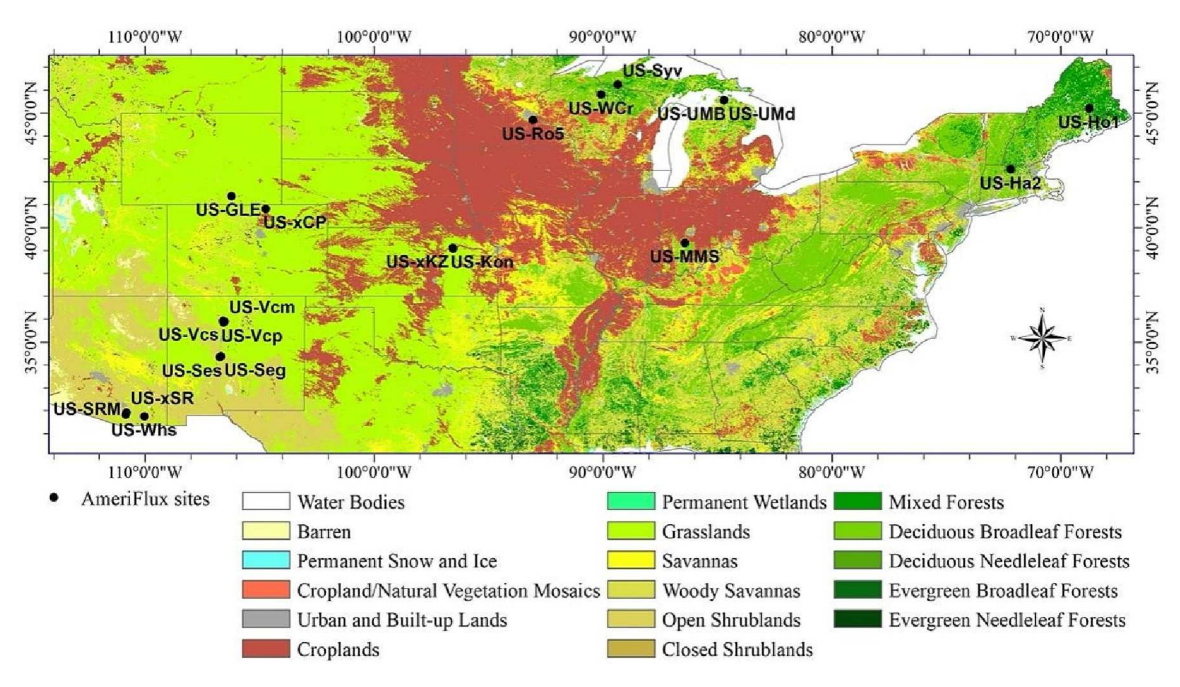


Fig. 13. Spatial distribution of the 20 AmeriFlux validation sites taking the 500 m-resolution MCD12Q1 yearly IGBP land cover classification in 2018 as a base map.

**Table 3**Summary of the 20 AmeriFlux validation sites.

Representativeness level	Number of sites	Site ID	Latitude, Longitude	Elevation (m)	IGBP Landcover	Temporal resolution (minutes)	Period
	1	US-SRM	31.8214°N, 110.8661°W	1120	WSA	30	2018–2019
	2	US-Ses	34.3349°N, 106.7442°W	1604	OSH	30	2018–2019
High	3	US-xSR	31.9107°N, 110.8355°W	983	OSH	30	2018–2019
	4	US-Kon	39.0824°N, 96.5603°W	417	GRA	30	2018.01–2018.10
	5	US-Seg	34.3623°N, 106.7019°W	1622	GRA	30	2018–2019
	6	US-Whs	31.7438°N, 110.0522°W	1370	OSH	30	2018–2019
	7	US-xCP	40.8155°N, 104.7456°W	1654	GRA	30	2018–2019
	8	US-xKZ	39.1008°N, 96.5631°W	381	GRA	30	2018–2019
Moderate	9	US-Ro5	44.6910°N, 93.0576°W	283	CRO	30	2018–2019
	10	US-Syv	46.2420°N, 89.3477°W	540	MF	30	2018.01–2018.11 & 2019.08–2019.12
	11	US-WCr	45.8059°N, 90.0799°W	520	DBF	30	2018–2019
	12	US- MMS	39.3232°N, 86.4131°W	275	DBF	60	2018–2019
	13	US- UMB	45.5598°N, 84.7138°W	234	DBF	30	2018–2019
	14	US- UMd	45.5625°N, 84.6975°W	239	DBF	30	2018–2019
	15	US-Vcm	35.8884°N, 106.5321°W	3003	ENF	30	2018–2019
	16	US-Vcp	35.8624°N, 106.5974°W	2542	ENF	30	2018–2019
	17	US-Vcs	35.9193°N, 106.6142°W	2752	ENF	30	2018–2019
	18	US-GLE	41.3665°N, 106.2399°W	3197	ENF	30	2018–2019
	19	US-Ha2	42.5393°N, 72.1779°W	360	ENF	30	2018–2019
	20	US-Ho1	45.2041°N, 68.7402°W	60	ENF	30	2018.01–2018.06

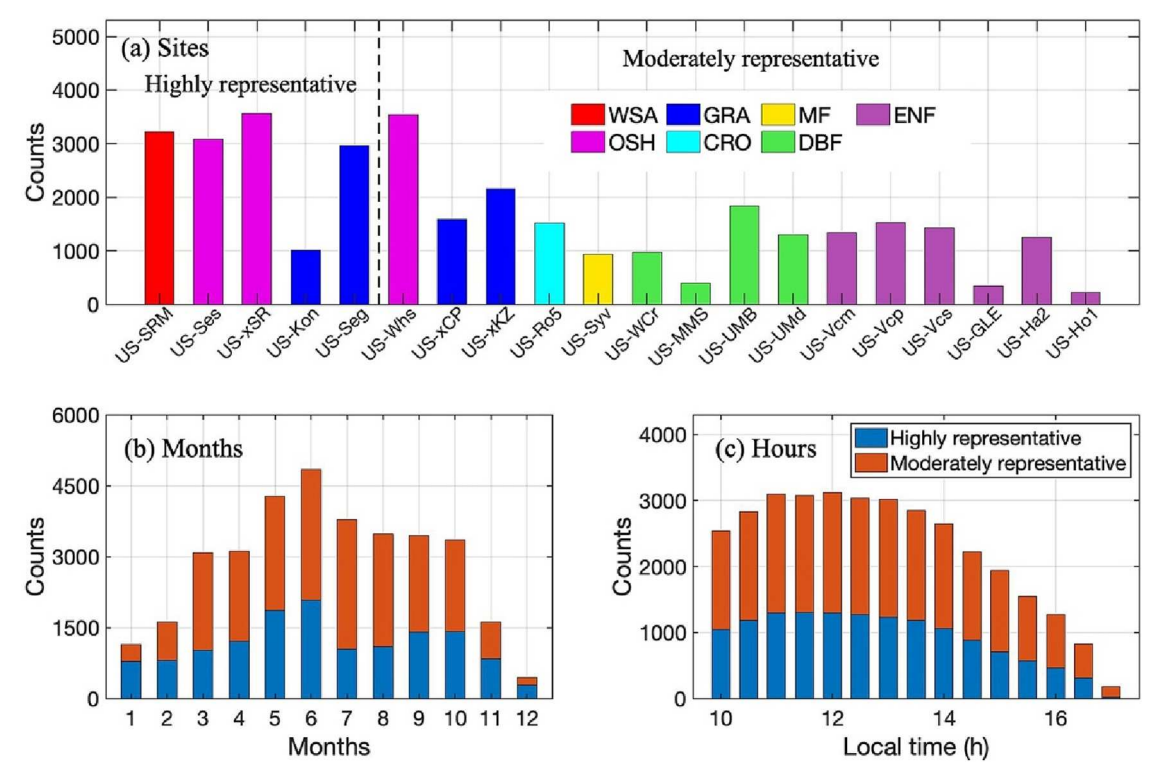
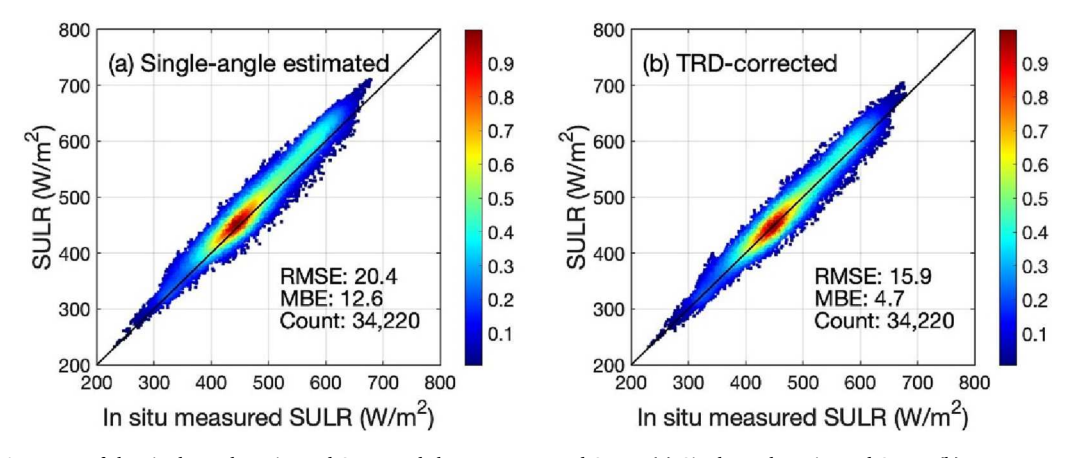


Fig. 14. Histograms of the number of validation data points in different sites, months, and local times.



 $\textbf{Fig. 15.} \ \ \textbf{Accuracy of the single-angle estimated SULR and the TRD-corrected SULR. (a) Single-angle estimated SULR. (b) TRD-corrected SULR.}$ 

## 4.3. Validation results with ABI/GOES-16 data and AmeriFlux in situ measurements

### 4.3.1. Accuracy with all data

The density scatter plots between the in situ measured SULR and the single-angle estimated SULR and TRD-corrected SULR are presented in Fig. 15. It can be found that the 34,220 groups of SULR validation data covered a wide range from 231.3 W/m² in winter to 678.9 W/m² in summer. The single-angle estimated SULR had an obvious positive MBE of 12.6 W/m² due to the TRD effect in the daytime. After correcting the TRD effect with the time-evolving KDM, the MBE was reduced to 4.7 W/m² with an improvement of 7.9 W/m² (62.7%). Furthermore, the RMSE of the single-angle estimated SULR was 20.4 W/m², which is similar to the daytime validation results of previous research based on polar orbiting satellite observations (Qin et al., 2020; Zeng et al., 2020). The overall RMSE value after the TRD correction was reduced to 15.9 W/m² with a significant improvement of 4.5 W/m² (22.1%).

### 4.3.2. Accuracy in different seasons

The accuracy of the time-evolving KDM was further evaluated in different seasons (Fig. 16). The SULR ranges varied among the different seasons. Spring had the widest SULR range of [231.3, 640.2]  $W/m^2$ , followed by autumn with a SULR range of [246.3, 636.6]  $W/m^2$  and then by summer with a SULR range of [372.3, 678.9]  $W/m^2$ . Winter had the smallest SULR range of [251.4, 509.3]  $W/m^2$ . In addition, summer and winter had the highest and lowest average SULR values, respectively.

The MBEs of the single-angle estimated SULR for the four seasons were all positive. The MBEs for the four seasons were 15.4 W/m² (spring), 11.0 W/m² (summer), 13.8 W/m² (fall), and 6.2 W/m² (winter). After correcting the TRD effect, the MBEs were reduced to 6.8 W/m², 3.2 W/m², 5.9 W/m² and 0.2 W/m² with improvements of 8.6 W/m² (55.8%), 7.8 W/m² (70.1%), 7.9 W/m² (57.2%) and 6.0 W/m² (96.8%) for spring, summer, fall and winter, respectively.

The RMSEs of the single-angle estimated SULR were 21.1 W/m<sup>2</sup>,

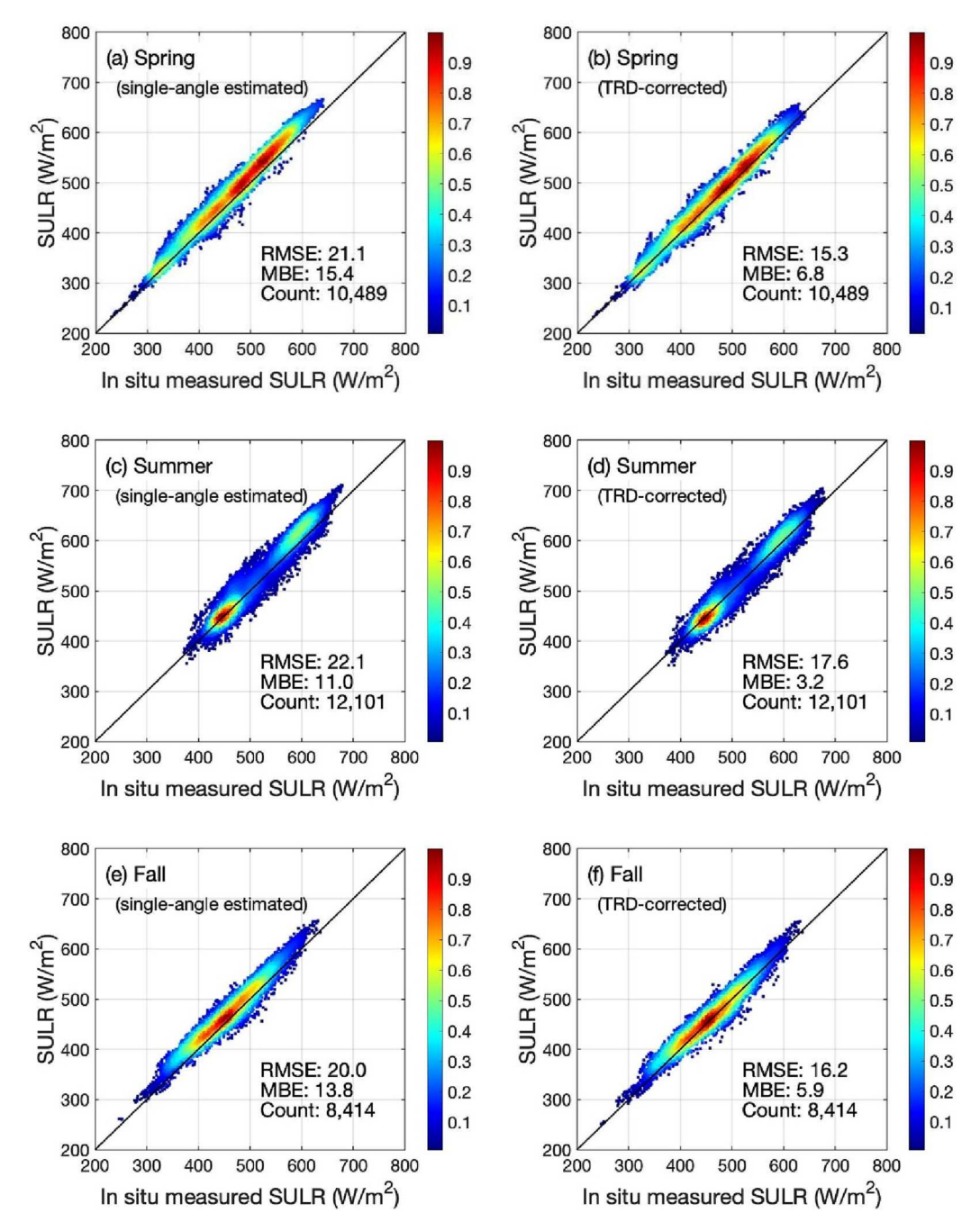


Fig. 16. Accuracy of the single-angle estimated SULR and the TRD-corrected SULR in the four seasons. (a-b) Spring. (c-d) Summer. (e-f) Fall. (g-h) Winter.

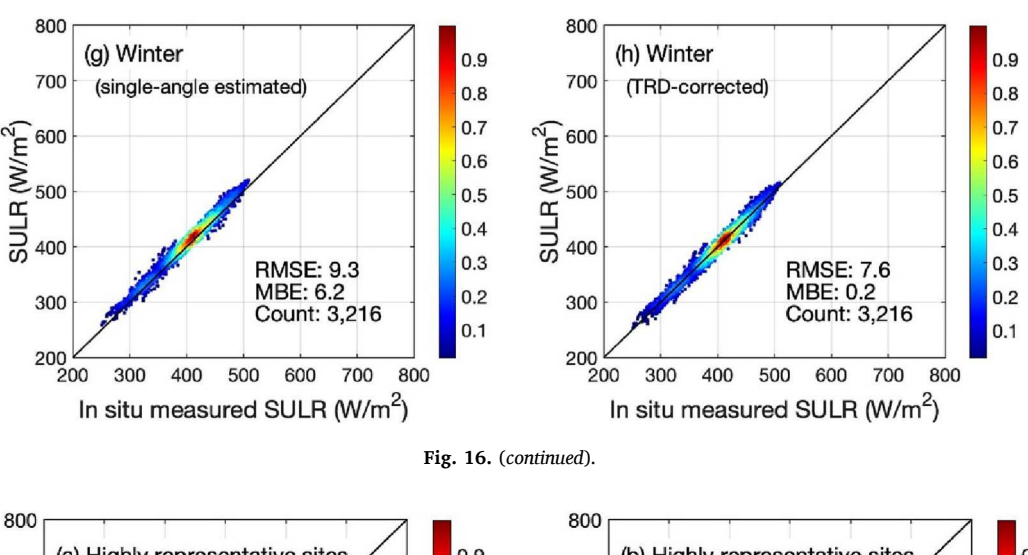
22.1 W/m², 20.0 W/m², and 9.3 W/m² for spring, summer, fall, and winter, respectively. After correcting the TRD effect, the RMSEs were reduced to 15.3 W/m², 17.6 W/m², 16.2 W/m², and 7.6 W/m² with improvements of 5.8 W/m² (27.5%), 4.5 W/m² (20.4%), 3.8 W/m² (19.0%) and 1.7 W/m² (18.3%), respectively. The outstanding ability of the time-evolving KDM in correcting the TRD effect of SULR was proven in all four seasons in this study.

### 4.3.3. Accuracy at different levels of representativeness

The 20 selected validation sites included five highly representative sites and 15 moderately representative sites as introduced in Table 3. We further studied the validation results at different levels of representativeness (see Fig. 17). The validation data from the highly representative sites covered a SULR range of [307.7, 678.9]  $\text{W/m}^2$  while the range for

the moderately representative sites was [231.3, 645.3]  $W/m^2$ . For the data from the five highly representative sites, the RMSE and MBE of the single-angle estimated SULR reached 21.1  $W/m^2$  and 15.6  $W/m^2$ , respectively, and after correcting the TRD effect, the RMSE and MBE were reduced to 15.1  $W/m^2$  and 5.7  $W/m^2$ , respectively, with corresponding improvements of 6.0  $W/m^2$  (28.4%) and 9.9  $W/m^2$  (63.4%).

For the data from the 15 moderately representative sites, the RMSE and MBE of the single-angle estimated SULR were 19.9 W/m² and 10.6 W/m², respectively. They are lower than those for the highly representative sites. After implementing the TRD correction, the RMSE and MBE of the moderately representativeness sites were reduced to 16.3 W/m² and 4.0 W/m², respectively, with corresponding improvements of 3.6 W/m² (18.1%) and 6.6 W/m² (62.3%). The slightly greater accuracy improvements at the highly representative sites are likely due to the



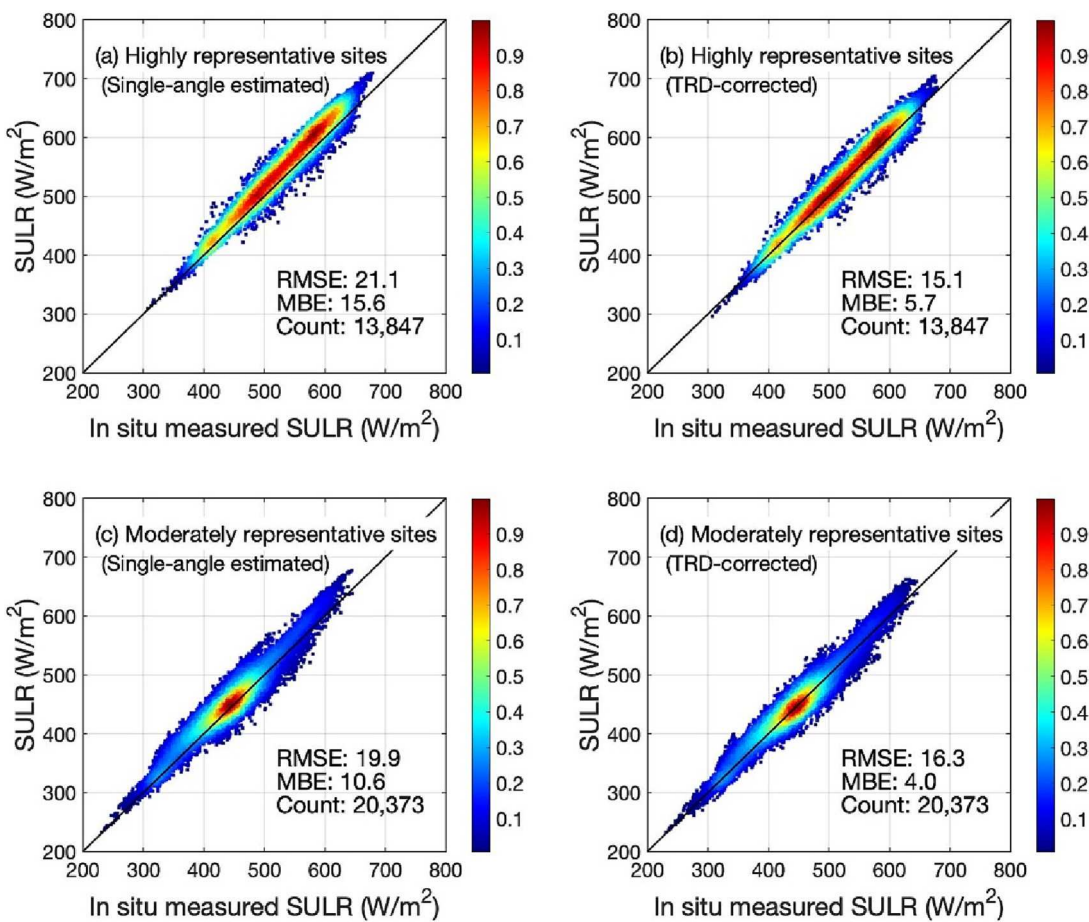


Fig. 17. Accuracy of the single-angle estimated SULR and the TRD-corrected SULR at different levels of representativeness. (a-b) Highly representative sites. (c-d) Moderately representative sites.

relatively higher representativeness of these five sites.

### 4.3.4. Accuracy for different sites and land cover categories

The performance of the time-evolving KDM for different sites and different land cover classes was further analyzed as plotted in Fig. 18. As shown in Fig. 18a, the RMSEs of the single-angle estimated SULR among the 20 sites ranged from 9.7 W/m $^2$  to 34.0 W/m $^2$ , which decreased to [6.9, 26.0] W/m $^2$  after the TRD correction. Sixteen sites showed a RMSE decrease of [0.5, 8.3] W/m $^2$ . Meanwhile, the RMSEs of four moderately representative sites (US-xKZ, US-Ro5, US-Syv, and US-UMd) had a slight RMSE increase of [0.03, 2.2] W/m $^2$ . This may explain by the relatively

lower RMSE values at these four sites  $(10.5-16.6 \text{ W/m}^2)$  and the relatively lower representativeness of these four sites.

Fig. 18b indicates that the |MBE| range of the single-angle estimated SULR among the 20 sites was [0.2, 30.4]  $W/m^2$ , which was reduced to [0.5, 22.6]  $W/m^2$  after correcting the TRD effect. Fifteen sites exhibited a significant reduction in the |MBE|, with a decrease of [3.5, 10.0]  $W/m^2$ . On the other hand, five moderately representative sites (US-xKZ, US-Ro5, US-Syv, US-WCr, and US-UMd) had an |MBE| increase of [3.3, 6.8]  $W/m^2$ , which was attributed to the relatively lower TRD effect at these sites. The single-angle estimated |MBE| values at these five sites were <2  $W/m^2$ .

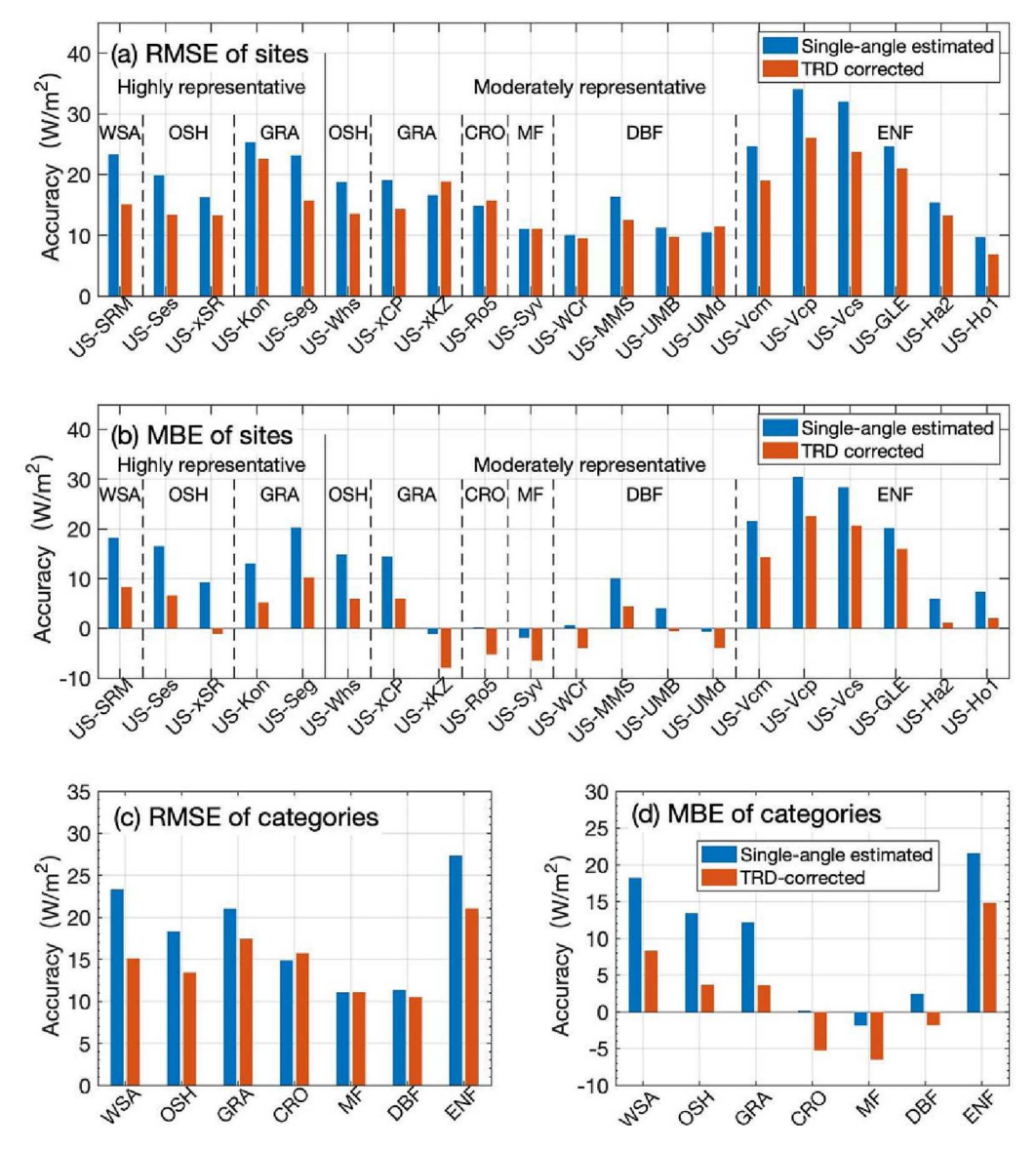


Fig. 18. Accuracy histograms of the single-angle estimated SULR and the TRD-corrected SULR at different sites and in different categories. (a-b) Histograms of the RMSE and MBE at different sites. (c-d) Histograms of the RMSE and MBE in different categories.

As shown in Fig. 18c, the RMSE range of the single-angle estimated SULR among the seven land cover types was [11.1, 27.4] W/m², which decreased to [10.5, 21.0] W/m² after applying the TRD correction. The RMSE of five land cover types (WSA, OSH, GRA, DBF and ENF) decrease by [0.9, 8.2] W/m² after the TRD correction, while the CRO and MF slightly increased by 0.03 W/m² and 0.9 W/m², respectively. This may be due to the relatively lower RMSEs (<15 W/m²) for these two land cover types. Likewise, Fig. 18d reveals that the |MBE| range of the single-angle estimated SULR among the seven land cover types was [0.2, 21.6] W/m², which was reduced to [1.8, 14.8] W/m² after the TRD correction. The |MBE| of the same five land cover types decreased by [0.7, 9.9] W/m² after correcting the TRD effect, while the CRO and MF increased by 5.1 W/m² and 4.6 W/m² from a |MBE| < 2 W/m².

### 4.3.5. Accuracy at different local times

We studied the performance of the time-evolving KDM at different local times, as the TRD effect is closely related to the surface thermal state which exhibits an obvious time-dependent tendency. Fig. 19 illustrates the fact that the MBE and RMSE of the single-angle estimated SULR clearly showed a diurnal variation in the daytime with an increasing trend from 10:00 to 10:30 and a decreasing trend from 10:30

to 17:00. The MBE and RMSE ranges of the single-angle estimated SULR were [1.4, 16.7]  $W/m^2$  and [12.5, 22.8]  $W/m^2$ , respectively. Furthermore, the maximum MBE and RMSE of the single-angle estimated SULR from the satellite dataset occurred in the morning (10:30). This was because the subpoint of GOES-16 was southeast of the 20 validation sites and the minimum phase angle (i.e., the angle distance between the illumination angle and viewing angle) occurred in the morning, leading to the relatively high TRD values in the morning.

After implementing the TRD correction, the diurnal variation trends of the MBE and RMSE were almost completely eliminated. The |MBE| of the TRD-corrected SULR was within the range of [0.6, 5.7] W/m² with improvements ranging from 0.8 (at 17:00) to 12.5 W/m² (at 10:30) compared with the single-angle estimated SULR. Likewise, the RMSE of the TRD-corrected SULR was within the range of [12.8, 17.0] W/m² with improvements ranging from 1.1 W/m² (at 16:30) to 7.3 W/m² (at 10:30) at 10:00–16:30. At 17:00, the RMSE had slightly increased by 0.7 W/m². The overall significant post-correction accuracy improvements reflect the excellent TRD correction ability of the proposed time-evolving KDM.

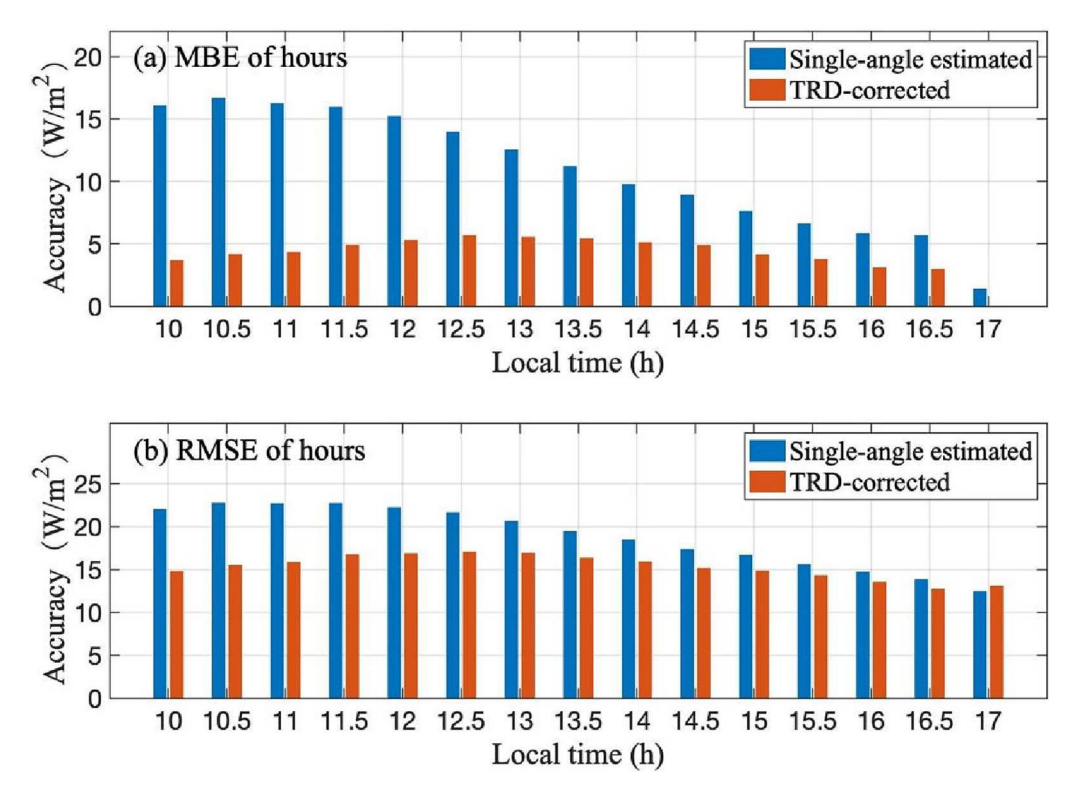


Fig. 19. Accuracy histograms of the single-angle estimated SULR and the TRD-corrected SULR at different local times. (a) MBE at different local times. (b) RMSE at different local times.

### 5. Conclusion

In this study, we proposed a six-parameter time-evolving KDM containing a four-parameter SULR DVM and a two-parameter TRD amplitude model to correct the TRD effect for geostationary satellite SULR datasets for the first time. The significant daytime TRD effect when solar zenith angle is within  $60^\circ$  can be effectively eliminated. The new KDM innovatively uses multi-temporal observations in a day to correct the TRD effect, not using multiangle observations at a specific time as in the past. The six parameters can be regressed with not less than six daytime single-angle estimated SULR values. The proposed time-evolving KDM was validated with a DART-simulated dataset (showing as an  $\rm R^2>0.999$  and a small RMSE  $=1.5~\rm W/m^2$ ); while the TRD correction method was comprehensively validated using two years of ABI data from the GOES-16 satellite and corresponding in situ measurements from 20 AmeriFlux sites. Three main conclusions about the TRD correction can be drawn as follows:

- (1) The TRD effect leads to the significant uncertainty of single-angle estimated SULR of geostationary satellites in the daytime. The RMSE and MBE of the single-angle estimated SULR can reach 20.4 W/m<sup>2</sup> and 12.6 W/m<sup>2</sup> for the GOES-16 satellite dataset, respectively.
- (2) The proposed time-evolving KDM can greatly mitigate the TRD-resulted uncertainty of the single-angle estimated SULR. For the satellite dataset, the RMSE decreased by 4.5 W/m $^2$  (22.1%), and the MBE dropped by 7.9 W/m $^2$  (62.7%).
- (3) The TRD effect leads to a phenomenon that the MBE and RMSE of the single-angle estimated SULR showed a diurnal variation in the daytime with relatively higher values around noon and lower values in the early morning and late afternoon. The time-evolving KDM reduced the MBE and RMSE at most of the studied local times except late afternoon with relatively less TRD effect.

The TRD effect is one of the main sources of error in the estimation of

surface thermal-related parameters from satellite remote sensing. This study demonstrates the possibility of using multi-temporal observations to correct the TRD effect for geostationary satellite data. This newly proposed TRD correction method has two limitations which will be the main focuses in the near future. First, the time-evolving KDM cannot be applied to high-latitude areas (e.g., polar regions) because these regions cannot be observed by geostationary satellites. Second, the proposed time-evolving KDM is not applicable for nighttime, since the TRD anisotropy is dominated by the angular-dependent emissivity at nighttime, not the hotspot signature at daytime. Further studies should focus on the development of new time-evolving KDM for multi-temporal polar-orbiting satellite observations over polar regions and new timeevolving KDM without hotspot kernel contribution for nighttime observations to overcome the limitations. The time-evolving KDM was evaluated on flat vegetated surface in this work, and the performance of this model on barren pixel and terrain surface still needs further studies in the future. The hybrid method of SULR estimation should also be evaluated through DART-based full-chain evaluation in the future. In addition, time-evolving KDMs with lower requirements of input observations (e.g., <6 clear-sky observations) are expected for better operationality in the TRD correction of geostationary satellite products.

### **Author contribution statement**

Boxiong Qin: Methodology, Programming, Writing, Original Draft Preparation.

Biao Cao: Conceptualization, Methodology, Reviewing and Editing. Jean-Louis Roujean: Methodology, Reviewing and Editing.

Jean-Philippe Gastellu-Etchegorry: Software, Reviewing and Editing. Sofia L. Ermida: Validation, Reviewing and Editing.

Zunjian Bian: Methodology.

Yongming Du: Methodology.

Tian Hu: Methodology.

Hua Li: Validation.

Qing Xiao: Validation.

Shuisen Chen: Validation.

Qinhuo Liu: Methodology, Funding acquisition.

### **Declaration of Competing Interest**

The authors declare that they have no known competing financial interests or personal relationships that could have appeared to influence the work reported in this paper.

### Data availability

Data will be made available on request.

### Acknowledgments

This work was supported in part by the National Natural Science

Foundation of China under Grant 41930111, 41871258, 42130104, 42130111, 42071317, 42271362; in part by the National Key Research and Development Program of China under Grant 2018YFA0605503; in part by the Youth Innovation Promotion Association CAS under Grant 2020127; in part by the "Future Star" Talent Plan of the Aerospace Information Research Institute of Chinese Academy of Sciences under Grant Y920570Z1F; in part by CAS President's International Fellowship for Visiting Scientists under Grant 2017VCA0034, 2017VCC0011 and 2019DC0020; in part by the Guangzhou Basic Research Project under Grant 202002020076; in part by GDAS' Project of Science and Technology Development under Grant 2022GDASZH-2022010102; in part by China Postdoctoral Science Foundation under Grant 2022M720846. We would like to thank the editors and four anonymous reviewers for their constructive comments and valuable suggestions.

### Appendix I. Single-angle SULR estimation with the hybrid method

The hybrid method directly estimates the SULR from TOA radiances with a predefined model. The model coefficients could be calculated through extensive radiative transfer simulations and regression (Wang et al., 2009), which bypasses the step of separating the LST and land surface emissivity but can achieve a comparable (or even superior) accuracy compared with the traditional physical method (Jiao et al., 2015; Cheng and Liang, 2016). The linear hybrid estimation method was used in this study with Eq. (I.1).

$$SULR_{dir} = a_{0,\theta_v} + a_{1,\theta_v} \cdot L_{TOA,11} + a_{2,\theta_v} \cdot L_{TOA,14} + a_{3,\theta_v} \cdot L_{TOA,15}$$
(I.1)

where  $\theta_{\nu}$  is the VZA,  $a_{0,\theta_{\nu}}$ - $a_{3,\theta_{\nu}}$  are the four regression coefficients at  $\theta_{\nu}$ , and  $L_{TOA,11}$ ,  $L_{TOA,14}$ , and  $L_{TOA,15}$  are the ABI TOA radiances in bands 11 (8.55  $\mu$ m), 14 (11.2  $\mu$ m), and 15 (12.3  $\mu$ m), respectively.

The regression of the model coefficients is based on a representative simulated dataset containing single-angle SULR ( $SULR'_{dir}$ ) and ABI TOA radiances ( $L'_{TOA,11}, L'_{TOA,14}$ , and  $L'_{TOA,15}$ ) using Eqs. (I.2–4). The inputs include the spectral surface emissivity ( $\varepsilon(\lambda)$ ), surface thermal emission calculated by Planck's law at the equivalent surface temperature  $T(B(\lambda,T))$ , three atmospheric parameters (i.e. atmospheric spectral transmittance  $\tau(\lambda)$ , upwelling radiance  $L_{\uparrow}(\lambda)$ , and downwelling radiance  $L_{\downarrow}(\lambda)$ ) and the sensor spectral response function ( $SRF(\lambda)$ ).

$$SULR'_{dir} = \pi \int_{1}^{100} I_{ground-leaving}(\lambda) d\lambda$$
 (1.2)

$$I_{ground-leaving}(\lambda) = \varepsilon(\lambda)B(\lambda, T) + (1 - \varepsilon(\lambda))L_{\downarrow}(\lambda) \tag{I.3}$$

$$L_{TOA,i}^{'} = \frac{\int_{\lambda_{1}}^{\lambda_{2}} \left(I_{ground-leaving}(\lambda)\tau(\lambda) + L_{\uparrow}(\lambda)\right) SRF_{i}(\lambda)d\lambda}{\int_{\lambda_{1}}^{\lambda_{2}} SRF_{i}(\lambda)d\lambda}, i \in [11, 14, 15]$$
(I.4)

where  $I_{ground-leaving}(\lambda)$  is the angle-independent spectral ground-leaving radiance,  $\lambda_1$  and  $\lambda_2$  are the spectral range boundaries for band i ( $i \in [11,14,15]$ ), and  $SRF_i(\lambda)$  is the spectral response function of band i.

Representative database of emissivity, atmospheric profiles, and LST ranges were important to the composition of  $SULR_{dir}$  and  $L_{TOA,i}$ . Here, the database are the same as that of Qin et al. (2020), except the  $SRF_i(\lambda)$  values. We used 35 typical surface emissivities from the MODIS UCSB spectral library (Li et al., 2013), including three for water, one for ice, one for snow, 13 for soils and minerals, and 17 for vegetation, and then extrapolated the emissivity value of above 14  $\mu$ m using method proposed by Wang et al. (2005). We selected 946 clear-sky atmospheric profiles from the TIGR database (Chevallier et al., 1998) with the criterion that the relative humidity in all layers should be <90% (Hu et al., 2017; Qin et al., 2020) and input the profiles into the MODTRAN model (Berk et al., 2003) to calculate the atmospheric parameters (i.e.,  $\tau(\lambda)$ ,  $L_{\downarrow}(\lambda)$ , and  $L_{\uparrow}(\lambda)$ ). The LSTs defined with a [-10, 15] K offset to the bottom temperature of the selected atmospheric profiles in a step of 5 K were input into Planck's function to calculate the spectral radiance (i.e.,  $B(\lambda, T)$ ). A simulation database containing 198,660 groups of SULR data ( $SULR_{dir}$ ) and corresponding TOA radiances ( $L_{TOA,i}$ ) was generated.

Next, the SULR estimation coefficients of Eq. (I.1) were generated using multiple linear regression. The coefficients were generated at different VZAs from  $0^{\circ}$  to  $60^{\circ}$  with a  $10^{\circ}$  step. The coefficients and the corresponding theoretical accuracies ( $R^2$ , MBE, and RMSE) are summarized in Table I.1, which shows that the hybrid method exhibits good accuracy with  $R^2 > 0.988$ , the MBEs are close to  $0 \text{ W/m}^2$ , and the RMSEs range from  $6.9 \text{ to } 11.3 \text{ W/m}^2$  with different VZAs. Then, the model coefficients ( $a_{0,\theta_v}$ - $a_{3,\theta_v}$ ) and the ABI observed clear-sky TOA radiances ( $L_{TOA,11}$ ,  $L_{TOA,14}$ , and  $L_{TOA,15}$ ) were input into the predefined single-angle SULR model (i.e., Eq. (I.1)) to estimate  $SULR_{dir}$ . It should be noted that the SULR value at a specific VZA was calculated with the interpolation or extrapolation of SULR values calculated with the coefficients at adjacent VZAs.

Table I.1 List of the coefficients and accuracies (unit:  $W/m^2$ ) for the single-angle SULR estimation.

$\theta_{ m v}$	$a_0$	$a_1$	$a_2$	<i>a</i> <sub>3</sub>	$R^2$	MBE	RMSE
<b>0</b> °	92.723	4.233	110.453	-81.722	0.996	0.00	6.9
10°	93.235	4.261	111.120	-82.543	0.996	0.00	7.0
20°	94.832	4.363	113.157	-85.072	0.995	0.00	7.2
30°	97.738	4.595	116.700	-89.544	0.995	0.00	7.6
40°	102.392	5.099	121.960	-96.391	0.994	0.00	8.3
$50^{\circ}$	109.601	6.217	129.165	-106.296	0.992	0.00	9.4
$60^{\circ}$	120.967	8.896	138.444	-120.497	0.988	0.00	11.3

### Appendix II. The rationale of modeling SULR diurnal variation using the same formatted equation as LST DTC

The SULR is the 4th power of LST and also contains the surface reflected downward longwave radiation (DLR) (i.e.,  $SULR = \varepsilon_{bb} \bullet \sigma \bullet LST^4 + (1 - \varepsilon_{bb}) \bullet DLR$ , where the  $\sigma$  is Stefan–Boltzmann constant (5.67 ×  $10^{-8}$  W/m²/K⁴) and the  $\varepsilon_{bb}$  is the broadband emissivity). The tendency of SULR is much closer to  $\sigma \bullet LST^4$  than to DLR considering their significant different weights ( $\varepsilon_{bb}$  vs  $1-\varepsilon_{bb}$ ). Furthermore, as shown in Fig. II.1 bellow, the SULR can be treated as a linear function of LST in the normal Earth surface temperature range of [260 K, 320 K]. The linear function fitting has a high R² = 0.993 which means that it's acceptable to model the SULR DVM using the same formatted equation as LST DTC. The R² is expected to be higher for one specific day since the LST range with in one day is usually <60 K (i.e., 320 K – 260 K in Fig. II.1).

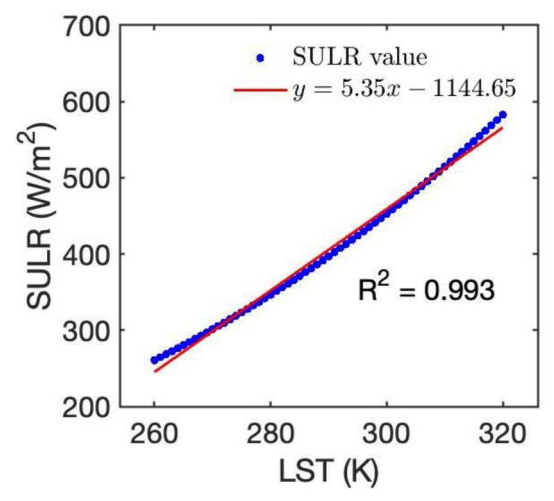


Fig. II.1. The linear fitting result between the SULR and LST values for a normal Earth surface temperature range (LST  $\in$  [260, 320] K). The  $\varepsilon_{bb}$  and DLR in calculating SULR were set as 0.96 and 300 W/m<sup>2</sup>, respectively.

Then, the daily variation of  $SULR_{hem}(t)$  is parameterized with a four-parameter trigonometric diurnal variation model (i.e., DVM) referenced to the DTC model of LST. The accuracy of the  $SULR_{hem}(t)$  DVM was evaluated using 34,220 clear-sky in-situ SULR measurement data at 20 AmeriFlux sites in 2018–2019 at 10:00–17:00 (the same dataset used in section 4). Fig. II.2(a) shows the high fitting accuracy of  $SULR_{hem}(t)$  DVM, with a RMSE of 1.9 W/  $m^2$  and a  $R^2$  of 0.9994. Fig.II.2(b) shows the DVM fitting result of a typical clear-sky day (2018/07/16) at site US-Whs. The evaluation result shows that the SULR DVM has an acceptable modeling accuracy.

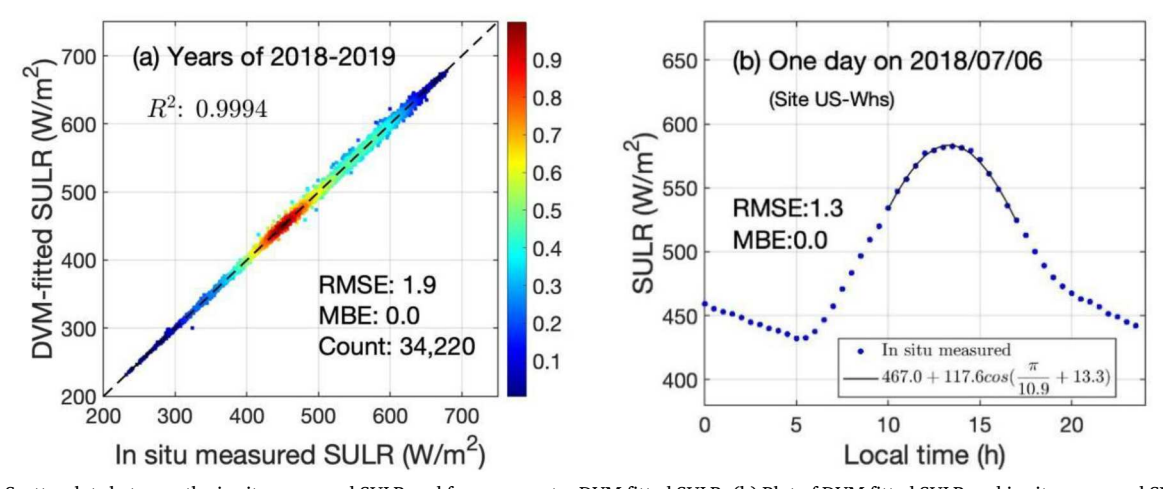


Fig. II.2. (a) Scatterplots between the in situ measured SULR and four-parameter DVM fitted SULR; (b) Plot of DVM fitted SULR and in situ measured SULR on 2018/07/16 at site US-Whs.

### Appendix III. Determination of the initial value and boundary of $\omega_{DTC}$ using synthetic dataset

The half-period parameter of LST DTC model (i.e.  $\omega_{DTC}$ ) can be determined by the duration of daytime (Göttsche and Olesen, 2001; Duan et al., 2012) using Eq.(III.1):

$$\omega_{DTC} = \frac{2}{15} arccos(-tan\phi tan\delta)$$
 (III.1)

where  $\phi$  is the latitude of the location,  $\delta$  is the solar declination that can be expressed as a function of the day of the year (*DOY*) (Elagib et al., 1999), which can be calculated by Eq.(III.2):

$$\delta = 23.45 \sin\left(\frac{360}{365}(284 + DOY)\right) \tag{III.2}$$

The half-period parameter of DVM model (i.e.,  $\omega_{DVM}$ ) is related to the  $\omega_{DTC}$  because the SULR is the 4th power of LST. To study the difference between  $\omega_{DVM}$  and  $\omega_{DTC}$ , five groups of DTC parameters of vegetation and soil (i.e.,  $T_0$ ,  $T_a$ ,  $\omega$ , and  $t_m$  in Eq.(III.3)) referenced to Liu et al. (2020b) were used to generate synthetic LST and SULR of mixed pixels. The DTC parameters were listed in Table III.1 (the same as Table 1 in Liu et al. (2020b)).

$$T(t) = T_0 + T_a \cdot \cos\left(\frac{\pi}{\alpha}(t - t_m)\right), t_{sr} \le t \le t_{ss}$$
(III.3)

**Table III.1**DTC parameters of five types of vegetation (V) and soil (S) of mixed pixels.

Parameters	Group 1		Group 2		Group 3		Group 4		Group 5	
	V	S	V	S	v	S	V	S	V	S
T <sub>0</sub> (K)	297.2	290.0	293.8	295.6	296.7	294.5	299.3	294.2	299.6	295.3
$T_a$ (K)	10.0	20.7	14.0	13.7	14.1	19.5	10.5	20.5	9.8	18.0
ω (h)	13.5	13.9	14.7	12.9	14.7	12.9	13.6	13.7	13.4	13.5
$t_m$ (h)	13.0	12.0	12.3	12.9	12.8	12.2	12.6	12.4	12.5	12.5

The LST of a vegetation and soil mixed pixel can be calculated using Eq. (III.4):

$$LST = \left(\frac{FVC \cdot \varepsilon_{\nu} \cdot T_{\nu}^{4} + (1 - FVC) \cdot \varepsilon_{s} \cdot T_{s}^{4}}{\varepsilon}\right)^{1/4}$$
(III.4)

where *FVC* is the fractional vegetation cover;  $\varepsilon_V$  and  $\varepsilon_S$  are the emissivity of vegetation (=0.98) and soil (=0.94), respectively;  $T_V$  and  $T_S$  are the component temperature of vegetation and soil, respectively;  $\varepsilon$  is the emissivity of the mixed pixel that can be calculated using Eq. (III.5):

$$\varepsilon = FVC \cdot \varepsilon_v + (1 - FVC) \cdot \varepsilon_s$$
 (III. 5)

To generate a representative dataset of LST, we set a range of reasonable offset to the *FVC* and the component temperature DTC parameters  $T_0$ ,  $T_{av}$  and  $\omega$  (see Table III.2). The  $t_m$  in Table III.1 is constant here since it has no influence in the  $\omega_{DTC}$ . In total, 36,300 groups of daily LST (5 groups of component temperatures, 11 groups of FVC values, 6 groups of  $T_0$ , 11 groups of  $T_0$ , and 10 groups of  $\omega$ ) could be generated.

**Table III.2**Parameters in generating representative LST dataset.

	FVC values	DTC parameters of components				
		$T_0$ values	$T_a$ values	$\omega$ values		
Minimum	0	T <sub>0</sub> -20	<i>T<sub>a</sub></i> - 5	ω - 6		
Step	0.1	5	1	1		
Maximum	1	$T_0 + 5$	$T_a + 5$	$\omega + 3$		

Then, the SULR values could be calculated using Eq. III.6 based on the generated LST, Stefan–Boltzmann constant  $\sigma$  (5.67 × 10<sup>-8</sup> W/m<sup>2</sup>/K<sup>4</sup>), broadband emissivity ( $\varepsilon_{bb}$ ) and atmospheric downwelling longwave radiation (*DLR*). The  $\varepsilon_{bb}$  and *DLR* were set to constant values of 0.96 and 300 W/m<sup>2</sup>, respectively.

$$SULR = \sigma \cdot \varepsilon_{bb} \cdot LST^4 + (1 - \varepsilon_{bb}) \cdot DLR \tag{III. 6}$$

Finally, the daily LST and SULR values were used to regress the LST half-period parameter (i.e.,  $\omega_{DTC}$ ) and the SULR half-period parameter (i.e.,  $\omega_{DVM}$ ). The scatterplot between the  $\omega_{DVM}$  and  $\omega_{DTC}$  was plotted in Fig. III.1(a), the histogram of half-period difference  $\Delta$  (i.e.,  $\Delta = \omega_{DVM} - \omega_{DTC}$ ) was shown in Fig. III.1(b). It could be found that the  $\omega_{DTC}$  calculated using the 36,300 groups of synthetic dataset covers a range of 6.9 to 17.7, and the  $\omega_{DVM}$  is always lower than  $\omega_{DTC}$  with a negative offset between -3.8 to -0.2. Therefore, to be more rational, the  $\omega_{DTC}$ -2 was used as the initial value of  $\omega_{DVM}$  and the boundary of  $\omega_{DVM}$  is set to be  $[\omega_{DTC} - 3.8$  to  $\omega_{DTC} - 0.2]$ .

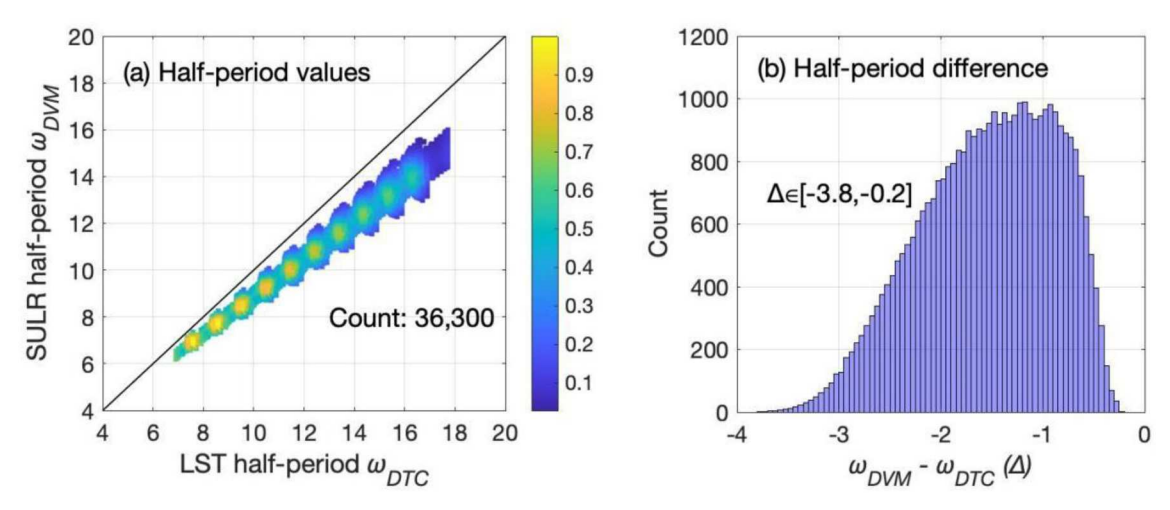


Fig. III.1. (a) scatterplot between LST half-period parameter  $\omega_{DVM}$  and SULR half-period parameter  $\omega_{DTC}$ ; (b) histogram of the half-period difference of  $\omega_{DVM} - \omega_{DTC}$ .

### Appendix IV. The sensitivity analysis of SULR to DLR variation in one day

The DLR ( $DLR = \sigma \bullet T_{atm}^4$ ,  $\sigma$  is Stefan–Boltzmann constant and the  $T_{atm}$  is atmosphere brightness temperature) is varied in one day, while is set as a constant in DART simulation in section 3.2. We analyze the sensitivity of SULR to DLR variation in a typical day. Fig. IV.1 shows the in-situ measured  $T_{atm}$  at AmeriFlux site US-Ses on 2018/04/01. A range of 8.8 K of diurnal DLR variation in local time 10:00–17:00 could be found.

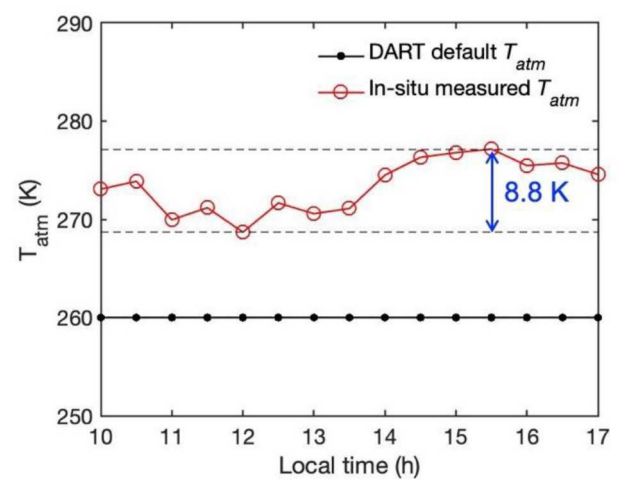


Fig. IV.1. In-situ measured  $T_{atm}$  of AmeriFlux site US-Ses on 2018/04/01.

The simulated SULR diurnal values with default  $T_{atm}$  and in-situ measured  $T_{atm}$  were compared in Fig. IV.2 (DART configuration: scene 2, component temperature group 1, location 1, see section 3.2). It shows that the SULR is insensitive to the diurnal variation of DLR with SULR differences  $\leq$ 0.87 W/m<sup>2</sup> in one day and it's acceptable to set the  $T_{atm}$  as a constant in DART simulations of SULR diurnal values.

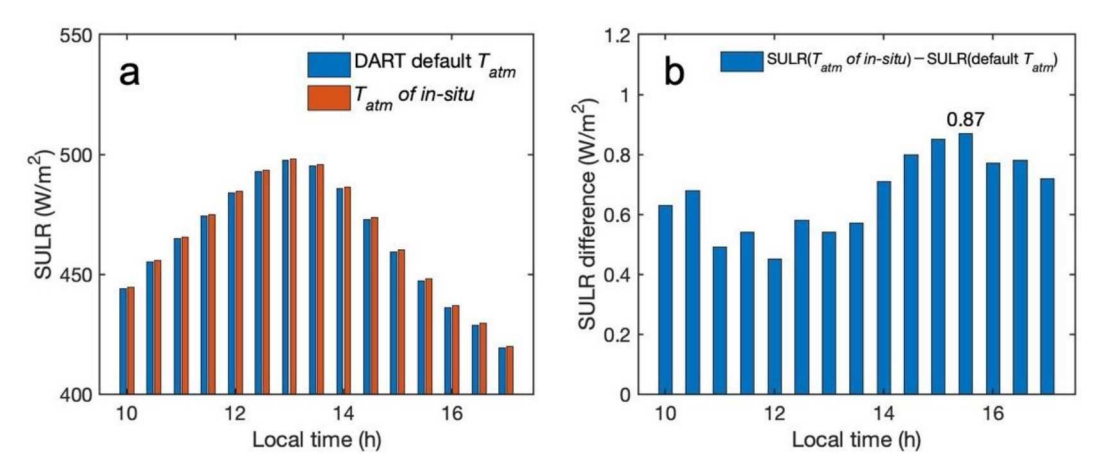


Fig. IV.2. DART-simulated SULR values (a) and their SULR differences (b).

#### References

- Berk, A., Anderson, G., Acharya, P., Hoke, M., Chetwynd, J., Bernstein, L., Shettle, E., Matthew, M., Adler-Golden, S., 2003. In: MODTRAN4 version 3 revision 1 user's manual. Air Force Research Laboratory, Space Vehicles Directoriate, Air Force Materiel Command, Hanscom AFB, MA, 1731, p. 3010.
- Bian, Z., Du, Y., Li, H., Cao, B., Huang, H., Xiao, Q., Liu, Q., 2017. Modeling the temporal variability of thermal emissions from row-planted scenes using a radiosity and energy budget method. IEEE Trans. Geosci. Remote Sens. 55, 6010–6026.
- Bian, Z., Roujean, J.-L., Lagouarde, J.-P., Cao, B., Li, H., Du, Y., Liu, Q., Xiao, Q., Liu, Q., 2020. A semi-empirical approach for modeling the vegetation thermal infrared directional anisotropy of canopies based on using vegetation indices. ISPRS J. Photogramm. Remote Sens. 160, 136–148.
- Bian, Z., Wu, S., Roujean, J.-L., Cao, B., Li, H., Yin, G., Du, Y., Xiao, Q., Liu, Q., 2022.
  A TIR forest reflectance and transmittance (FRT) model for directional temperatures with structural and thermal stratification. Remote Sens. Environ. 268, 112749.
- Cao, B., Gastellu-Etchegorry, J.-P., Du, Y., Li, H., Bian, Z., Hu, T., Fan, W., Xiao, Q., Liu, Q., 2019a. Evaluation of four kernel-driven models in the thermal infrared band. IEEE Trans. Geosci. Remote Sens. 57, 5456–5475.
- Cao, B., Guo, M., Fan, W., Xu, X., Peng, J., Ren, H., Du, Y., Li, H., Bian, Z., Hu, T., Xiao, Q., Liu, Q., 2018. A new directional canopy emissivity model based on spectral invariants. IEEE Trans. Geosci. Remote Sens. 56, 6911–6926.
- Cao, B., Liu, Q., Du, Y., Roujean, J.-L., Gastellu-Etchegorry, J.-P., Trigo, I.F., Zhan, W., Yu, Y., Cheng, J., Jacob, F., 2019b. A review of earth surface thermal radiation directionality observing and modeling: historical development, current status and perspectives. Remote Sens. Environ. 232, 111304.
- Cao, B., Roujean, J.-L., Gastellu-Etchegorry, J.-P., Liu, Q., Du, Y., Lagouarde, J.-P., Huang, H., Li, H., Bian, Z., Hu, T., Qin, B., Ran, X., Xiao, Q., 2021. A general framework of kernel-driven modeling in the thermal infrared domain. Remote Sens. Environ. 252, 112157.
- Chen, J., Black, T., 1991. Measuring leaf area index of plant canopies with branch architecture. Agric. For. Meteorol. 57, 1–12.
- Chen, J.M., Leblanc, S.G., 1997. A four-scale bidirectional reflectance model based on canopy architecture. Geosci.Remote Sens.IEEE Trans. 35, 1316–1337.
- Cheng, J., Liang, S., 2016. Global estimates for high-spatial-resolution clear-sky land surface upwelling longwave radiation from MODIS data. IEEE Trans. Geosci. Remote Sens. 54, 4115–4129.
- Chevallier, F., Chéruy, F., Scott, N.A., Chédin, A., 1998. A neural network approach for a fast and accurate computation of a longwave radiative budget. J. Appl. Meteorol. 37, 1385–1397.
- Chu, H., Luo, X., Ouyang, Z., Chan, W.S., Dengel, S., Biraud, S.C., Torn, M.S., Metzger, S., Kumar, J., Arain, M.A., Arkebauer, T.J., Baldocchi, D., Bernacchi, C., Billesbach, D., Black, T.A., Blanken, P.D., Bohrer, G., Bracho, R., Brown, S., Brunsell, N.A., Chen, J., Chen, X., Clark, K., Desai, A.R., Duman, T., Durden, D., Fares, S., Forbrich, I., Gamon, J.A., Gough, C.M., Griffis, T., Helbig, M., Hollinger, D., Humphreys, E., Ikawa, H., Iwata, H., Ju, Y., Knowles, J.F., Knox, S.H., Kobayashi, H., Kolb, T., Law, B., Lee, X., Litvak, M., Liu, H., Munger, J.W., Noormets, A., Novick, K., Oberbauer, S.F., Oechel, W., Oikawa, P., Papuga, S.A., Pendall, E., Prajapati, P., Prueger, J., Quinton, W.L., Richardson, A.D., Russell, E.S., Scott, R.L., Starr, G., Staebler, R., Stoy, P.C., Stuart-Haëntjens, E., Sonnentag, O., Sullivan, R.C., Suyker, A., Ueyama, M., Vargas, R., Wood, J.D., Zona, D., 2021. Representativeness

- of Eddy-covariance flux footprints for areas surrounding AmeriFlux sites. Agric. For. Meteorol. 301-302, 108350.
- Coleman, T.F., Li, Y., 1996. An interior trust region approach for nonlinear minimization subject to bounds. SIAM J. Optim. 6, 418–445.
- Coll, C., Galve, J.M., Niclòs, R., Valor, E., Barberà, M.J., 2019. Angular variations of brightness surface temperatures derived from dual-view measurements of the advanced along-track scanning radiometer using a new single band atmospheric correction method. Remote Sens. Environ. 223, 274–290.
- Cuenca, J., Sobrino, J.A., 2004a. Experimental measurements for studying angular and spectral variation of thermal infrared emissivity. Appl. Opt. 43, 4598.
- Cuenca, J., Sobrino, J.A., 2004b. Experimental measurements for studying angular and spectral variation of thermal infrared emissivity. Appl. Opt. 43, 4598–4602.
- Du, Y., Liu, Q., Chen, L., Liu, Q., Yu, T., 2007. Modeling directional brightness temperature of the winter wheat canopy at the ear stage. IEEE Trans. Geosci. Remote Sens. 45, 3721–3739.
- Duan, S.-B., Li, Z.-L., Wang, N., Wu, H., Tang, B.-H., 2012. Evaluation of six land-surface diurnal temperature cycle models using clear-sky in situ and satellite data. Remote Sens. Environ. 124, 15–25.
- Duffour, C., Lagouarde, J.P., Roujean, J.L., 2016. A two parameter model to simulate thermal infrared directional effects for remote sensing applications. Remote Sens. Environ. 186, 250–261.
- Dyce, D.R., Voogt, J.A., 2018. The influence of tree crowns on urban thermal effective anisotropy. Urban Clim. 23, 91–113.
- Elagib, N., Alvi, S., Mansell, M., 1999. Day-length and extraterrestrial radiation for Sudan: a comparative study. Int.J.Solar Energy 20, 93–109.
- Ermida, S.L., DaCamara, C.C., Trigo, I.F., Pires, A.C., Ghent, D., Remedios, J., 2017. Modelling directional effects on remotely sensed land surface temperature. Remote Sens. Environ. 190, 56–69.
- Ermida, S.L., Trigo, I.F., DaCamara, C.C., Pires, A.C., 2018. A methodology to simulate LST directional effects based on parametric models and landscape properties. Remote Sens. 10, 1114.
- Ermida, S.L., Trigo, I.F., Hulley, G., DaCamara, C.C., 2020. A multi-sensor approach to retrieve emissivity angular dependence over desert regions. Remote Sens. Environ. 237, 111550
- Francois, C., Ottle, C., Prevot, L., 1997. Analytical parameterization of canopy directional emissivity and directional radiance in the thermal infrared. Application on the retrieval of soil and foliage temperatures using two directional measurements. Int. J. Remote Sens. 18, 2587–2621.
- Friedl, M.A., McIver, D.K., Hodges, J.C.F., Zhang, X.Y., Muchoney, D., Strahler, A.H., Woodcock, C.E., Gopal, S., Schneider, A., Cooper, A., Baccini, A., Gao, F., Schaaf, C., 2002. Global land cover mapping from MODIS: algorithms and early results. Remote Sens. Environ. 83, 287–302.
- García-Santos, V., Coll, C., Valor, E., Niclòs, R., Caselles, V., 2015. Analyzing the anisotropy of thermal infrared emissivity over arid regions using a new MODIS land surface temperature and emissivity product (MOD21). Remote Sens. Environ. 169, 212–221.
- García-Santos, V., Valor, E., Caselles, V., Ángeles Burgos, M., Coll, C., 2012. On the angular variation of thermal infrared emissivity of inorganic soils. J.Geophys.Res. Atmos. 117, D19116.
- Garcia-Santos, V., Valor, E., Caselles, V., Coll, C., Burgos, M.A., 2014. Effect of soil moisture on the angular variation of thermal infrared emissivity of inorganic soils. IEEE Geosci. Remote Sens. Lett. 11, 1091–1095.

- Gastellu-Etchegorry, J.-P., Grau, E., Lauret, N., 2012. DART: A 3D model for remote sensing images and radiative budget of earth surfaces. Modeling and simulation in Engineering. ISBN 978-953-307-959-972.
- Gastellu-Etchegorry, J.-P., Yin, T., Lauret, N., Cajgfinger, T., Gregoire, T., Grau, E., Feret, J.-B., Lopes, M., Guilleux, J., Dedieu, G., 2015. Discrete anisotropic radiative transfer (DART 5) for modeling airborne and satellite spectroradiometer and LIDAR acquisitions of natural and urban landscapes. Remote Sens. 7, 1667-1701.
- Geiger, B., Carrer, D., Franchisteguy, L., Roujean, J., Meurey, C., 2008. Land surface albedo derived on a daily basis from Meteosat second generation observations. IEEE Trans. Geosci. Remote Sens. 46, 3841-3856.
- Ghent, D., Corlett, G., Göttsche, F.M., Remedios, J., 2017. Global land surface temperature from the along-track scanning radiometers. J.Geophys.Res.Atmos. 122, 12,167-112,193.
- Göttsche, F.-M., Olesen, F.S., 2001. Modelling of diurnal cycles of brightness temperature extracted from METEOSAT data. Remote Sens. Environ. 76, 337-348.
- Guillevic, P.C., Bork-Unkelbach, A., Göttsche, F.M., Hulley, G., Gastellu-Etchegorry, J.-P., Olesen, F.S., Privette, J.L., 2013. Directional viewing effects on satellite land surface temperature products over sparse vegetation canopies—a multisensor analysis. IEEE Geosci. Remote Sens. Lett. 10, 1464-1468.
- He, T., Zhang, Y., Liang, S., Yu, Y., Wang, D., 2019. Developing land surface directional Reflectance and Albedo products from geostationary GOES-R and Himawari data: theoretical basis, operational implementation, and validation. Remote Sens. 11,
- Hu, L., Monaghan, A., Voogt, J.A., Barlage, M., 2016a. A first satellite-based observational assessment of urban thermal anisotropy. Remote Sens. Environ. 181, 111-121.
- Hu, T., Cao, B., Du, Y., Li, H., Wang, C., Bian, Z., Sun, D., Liu, Q., 2017. Estimation of surface upward longwave radiation using a direct physical algorithm. IEEE Trans. Geosci. Remote Sens. 55, 4412-4426.
- Hu, T., Du, Y., Cao, B., Li, H., Bian, Z., Sun, D., Liu, Q., 2016b. Estimation of upward longwave radiation from vegetated surfaces considering thermal directionality. IEEE Trans. Geosci. Remote Sens. 54, 6644-6658.
- Hu, T., Renzullo, L.J., Cao, B., van Dijk, A.I., Du, Y., Li, H., Cheng, J., Xu, Z., Zhou, J., Liu, Q., 2019. Directional variation in surface emissivity inferred from the MYD21 product and its influence on estimated surface upwelling longwave radiation. Remote Sens. Environ. 228, 45–60.
- Jiang, L., Zhan, W., Hu, L., Huang, F., Hong, F., Liu, Z., Lai, J., Wang, C., 2021. Assessment of different kernel-driven models for daytime urban thermal radiation directionality simulation. Remote Sens. Environ. 263, 112562.
- Jiao, Z., Yan, G., Zhao, J., Wang, T., Chen, L., 2015. Estimation of surface upward longwave radiation from MODIS and VIIRS clear-sky data in the Tibetan plateau. Remote Sens. Environ. 162, 221–237.
- Lagouarde, J.-P., Irvine, M., 2008, Directional anisotropy in thermal infrared measurements over Toulouse city centre during the CAPITOUL measurement campaigns: first results. Meteorog. Atmos. Phys. 102, 173. Lagouarde, J.P., Hénon, A., Irvine, M., Voogt, J., Pigeon, G., Moreau, P., Masson, V.,
- Mestayer, P., 2012. Experimental characterization and modelling of the nighttime directional anisotropy of thermal infrared measurements over an urban area; case study of Toulouse (France). Remote Sens. Environ. 117, 19-33.
- Lagouarde, J.P., Hénon, A., Kurz, B., Moreau, P., Irvine, M., Voogt, J., Mestayer, P., 2010. Modelling daytime thermal infrared directional anisotropy over Toulouse city centre. Remote Sens. Environ. 114, 87-105.
- Li, Y., Coleman, T., 1994. On the convergence of reflective newton methods for largescale nonlinear minimization subject to bounds. Math. Program. 67, 189-224.
- Li, K., Qian, Y., Wang, N., Li, W., Qiu, S., Ma, L., Li, C., Sun, D., Liu, Y., Ni, L., 2022. A four-component parameterized directional thermal radiance model for row canopies. IEEE Trans. Geosci. Remote Sens. 60, 5000615.
- Li, Z.-L., Wu, H., Wang, N., Qiu, S., Sobrino, J.A., Wan, Z., Tang, B.-H., Yan, G., 2013. Land surface emissivity retrieval from satellite data. Int. J. Remote Sens. 34, 3084\_3127
- Liu, X., Tang, B., Li, Z., Rasmussen, M.O., 2020a. Influence of temperature inertia on thermal radiation directionality modeling based on geometric optical model. IEEE Trans. Geosci. Remote Sens. 58, 3445–3457.
- Liu, X., Tang, B.-H., Li, Z.-L., Zhou, C., Wu, W., Rasmussen, M.O., 2020b. An improved method for separating soil and vegetation component temperatures based on diurnal temperature cycle model and spatial correlation. Remote Sens. Environ. 248
- Liu, X., Tang, B.H., Li, Z.L., Zhang, X., Shang, G., 2020c. On the derivation of geometric optical kernels for directional thermal radiation. Earth SpaceSci. 7 e2019EA000895.
- Masuda, K., Takashima, T., Takayama, Y., 1988. Emissivity of pure and sea waters for the model sea surface in the infrared window regions. Remote Sens. Environ. 24, 313-329
- McGuire, M.J., Balick, L.K., Smith, J.A., Hutchison, B., 1989. Modeling directional thermal radiance from a forest canopy. Remote Sens. Environ. 27, 169-186.
- Minnis, P., Khaiyer, M.M., 2000. Anisotropy of land surface skin temperature derived from satellite data. J. Appl. Meteorol. 39, 1117-1129.
- Monteith, J.L., Szeicz, G., 1962. Radiative temperature in the heat balance of natural surfaces. Q. J. R. Meteorol. Soc. 88, 496-507.
- Otterman, J., Susskind, J., Brakke, T., Kimes, D., Pielke, R., Lee, T., 1995. Inferring the thermal-infrared hemispheric emission from a sparsely-vegetated surface by directional measurements. Bound.Layer Meteorol. 74, 163-180.
- Pérez-Planells, L., Niclòs, R., Valor, E., Göttsche, F.-M., 2022. Retrieval of land surface emissivities over partially vegetated surfaces from satellite data using radiative transfer models. IEEE Trans. Geosci. Remote Sens. 60, 1-21.

- Pinheiro, A.C., Privette, J.L., Guillevic, P., 2006. Modeling the observed angular anisotropy of land surface temperature in a savanna. IEEE Trans. Geosci. Remote Sens. 44, 1036–1047.
- Pinheiro, A.C., Privette, J.L., Mahoney, R., Tucker, C.J., 2004. Directional effects in a daily AVHRR land surface temperature dataset over Africa. IEEE Trans. Geosci. Remote Sens. 42, 1941-1954.
- Qi, J., Xie, D., Yin, T., Yan, G., Gastellu-Etchegorry, J.-P., Li, L., Zhang, W., Mu, X., Norford, L.K., 2019. LESS: LargE-scale remote sensing data and image simulation framework over heterogeneous 3D scenes. Remote Sens. Environ. 221, 695-706.
- Qin, B., Cao, B., Li, H., Bian, Z., Hu, T., Du, Y., Yang, Y., Xiao, Q., Liu, Q., 2020. Evaluation of six high-spatial resolution clear-sky surface upward longwave radiation estimation methods with MODIS. Remote Sens. 12, 1834.
- Rasmussen, M.O., Gottsche, F.-M., Olesen, F.-S., Sandholt, I., 2011. Directional effects on land surface temperature estimation from meteosat second generation for savanna landscapes. IEEE Trans. Geosci. Remote Sens. 49, 4458-4468.
- Ren, H., Liu, R., Yan, G., Mu, X., Li, Z.L., Nerry, F., Liu, Q., 2014. Angular normalization of land surface temperature and emissivity using multiangular middle and thermal infrared data. IEEE Trans. Geosci.Remote Sens. 52, 4913-4931.
- Roy, D.P., Zhang, H.K., Ju, J., Gomez-Dans, J.L., Lewis, P.E., Schaaf, C.B., Sun, Q., Li, J., Huang, H., Kovalskyy, V., 2016. A general method to normalize landsat reflectance data to nadir BRDF adjusted reflectance. Remote Sens. Environ. 176, 255-271.
- Schaaf, C.B., Gao, F., Strahler, A.H., Lucht, W., Li, X., Tsang, T., Strugnell, N.C., Zhang, X., Jin, Y., Muller, J.-P., Lewis, P., Barnsley, M., Hobson, P., Disney, M., Roberts, G., Dunderdale, M., Doll, C., d'Entremont, R.P., Hu, B., Liang, S., Privette, J. L., Roy, D., 2002. First operational BRDF, albedo nadir reflectance products from MODIS. Remote Sens. Environ. 83, 135-148.
- Sinnott, R.W., 1994. Astronomical computing: sunrise and sunset: a challenge. Sky and Telescope 88, 84-85.
- Sobrino, J.A., Cuenca, J., 1999. Angular variation of thermal infrared emissivity for some natural surfaces from experimental measurements. Appl. Opt. 38, 3931-3936.
- Sobrino, J.A., Jiménez-Muñoz, J.C., Verhoef, W., 2005. Canopy directional emissivity: comparison between models. Remote Sens. Environ. 99, 304-314.
- Tang, B., Li, Z.-L., 2008. Estimation of instantaneous net surface longwave radiation from MODIS cloud-free data. Remote Sens. Environ. 112, 3482–3492.
- Trigo, I.F., Monteiro, I.T., Olesen, F., Kabsch, E., 2008. An assessment of remotely sensed land surface temperature. J.Geophys.Res.Atmos. 113.
- Verhoef, W., Jia, L., Xiao, Q., Su, Z., 2007. Unified optical-thermal four-stream radiative transfer theory for homogeneous vegetation canopies. IEEE Trans. Geosci. Remote Sens. 45, 1808–1822.
- Vinnikov, K.Y., Yu, Y., Goldberg, M.D., Tarpley, D., Romanov, P., Laszlo, I., Chen, M., 2012. Angular anisotropy of satellite observations of land surface temperature. Geophys, Res. Lett. 39.
- Wang, D., Chen, Y., Hu, L., Voogt, J.A., Gastellu-Etchegorry, J.-P., Kravenhoff, E.S., 2021. Modeling the angular effect of MODIS LST in urban areas: A case study of Toulouse, France. Remote Sens.Environ. 257, 112361.
- Wang, D., Chen, Y., Voogt, J.A., Krayenhoff, E.S., Wang, J., Wang, L., 2020. An advanced geometric model to simulate thermal anisotropy time-series for simplified urban neighborhoods (GUTA-T). Remote Sens. Environ. 237, 111547.
- Wang, D., Chen, Y., Zhan, W., 2018. A geometric model to simulate thermal anisotropy over a sparse urban surface (GUTA-sparse). Remote Sens. Environ, 209, 263–274.
- Wang, K., Wan, Z., Wang, P., Sparrow, M., Liu, J., Zhou, X., Haginoya, S., 2005. Estimation of surface long wave radiation and broadband emissivity using Moderate Resolution Imaging Spectroradiometer (MODIS) land surface temperature/ emissivity products. J.Geophys.Res.Atmos. 110.
- Wang, W., Liang, S., Augustine, J.A., 2009. Estimating high spatial resolution clear-sky land surface upwelling longwave radiation from MODIS data. IEEE Trans.Geosci. Remote Sens. 47, 1559-1570.
- Wang, Y., Gastellu-Etchegorry, J.-P., 2021. Accurate and fast simulation of remote sensing images at top of atmosphere with DART-lux. Remote Sens. Environ. 256, 112311
- Wang, Y., Kallel, A., Yang, X., Regaieg, O., Lauret, N., Guilleux, J., Chavanon, E., Gastellu-Etchegorry, J.-P., 2022. DART-lux: an unbiased and rapid Monte Carlo radiative transfer method for simulating remote sensing images. Remote Sens. Environ. 274, 112973.
- Yang, P., Prikaziuk, E., Verhoef, W., van der Tol, C., 2021. SCOPE 2.0: a model to simulate vegetated land surface fluxes and satellite signals. Geosci. Model Dev. 14, 4697-4712.
- Zeng, Q., Cheng, J., Dong, L., 2020. Assessment of the Long-Term High-Spatial-Resolution Global LAnd Surface Satellite (GLASS) Surface Longwave Radiation Product Using Ground Measurements. IEEE J.Select.Top.Appl.Earth Observ.Remote Sens. 13, 2032-2055.

### Glossary

TRD: Thermal Radiation Directionality

SULR: Surface Upward Longwave Radiation

TOA: Top-of-Atmosphere

DBT: Directional Brightness Temperature

VNIR: Visible and Near InfraRed DVM: Diurnal Variation Model

VZA: Viewing Zenith Angle

SPP: Solar Principal Plane SAA: Solar Azimuth Angle

DTC: Diurnal Temperature Cycle

MBE: Mean Bias Error

LAI: Leaf Area Index WSA: Woody Savanna GRA: Grassland MF: Mixed Forest

ENF: Evergreen Needleleaf Forest

ATSR-2: Along-Track Scanning Radiometer - 2
SLSTR: Sea and Land Surface Temperature Radiometer DLR: Atmosphere downwelling longwave radiation

TIR: Thermal Infrared

LST: Land Surface Temperature
MODIS: Moderate Resolution Imaging Spectroradiometer

KDM: Kernel-driven Model SZA: Solar Zenith angle

ABI: Advanced Baseline Imager VAA: Viewing Azimuth Angle CSPP: Cross Solar Principal Plane BOA: Bottom-of-atmosphere RMSE: Root-mean-square error

DART: Discrete Anisotropic Radiative Transfer Model IGBP: International Geosphere Biosphere Programme

OSH: Open Shrubland CRO: Cropland

DBF: Deciduous Broadleaf Forest
ATSR: Along-Track Scanning Radiometer

AATSR: Advanced Along-Track Scanning Radiometer

STD: Standard derivation